공학석사 학위논문

An investigation into the manganese oxide nanoparticles for efficient oxygen evolution reaction: Effect of crystal structure and nano size on the catalytic activity

효율적인 산소 발생 반응을 위한 망간 산화물 나노 입자에 대한 연구: 재료의 결정구조와 나노 사이즈가 촉매 특성에 미치는 영향

2016년 2월

서울대학교 대학원

재료공학부

정 동 혁

Abstract

An investigation into the manganese oxide nanoparticles for efficient oxygen evolution reaction: Effect of crystal structure and nano size on the catalytic activity

Donghyuk Jeong
Department of Materials Science and Engineering
The Graduate School
Seoul National University

Development of outstanding oxygen evolution reaction(OER) catalyst is essential for efficient hydrogen gas production which is attractive sustainable energy in the future. For this reason, various manganese oxides with bulk scale have been developed and investigated. However, OER activity of conventional manganese oxides in neutral condition is still poor. Thus, our group solved the low activity issue of bulk manganese oxides by introducing MnO nanoparticles in previous research.

In this research, we tried to investigate the effect of crystal structure on the OER activity of manganese oxide nanoparticles for more activity

enhancement. To clearly see the effect of crystal structure, manganese oxide nanoparticles with various crystal structure(Mn_3O_4, Mn_5O_8 and Mn_2O_3) were obtained with little morphology change via the controlled oxidation of MnO nanoparticles. The oxygen evolution reaction (OER) properties of manganese oxide nanoparticles were evaluated using cyclic voltammetry (CV). Mn_3O_4 and Mn_2O_3 nanoparticles showed similar activity and Mn_5O_8 nanoparticles showed less active property than Mn_3O_4 and Mn_2O_3. This observation indicates that effect of crystal structure on OER activity of Mn oxides is significantly reduced in nano scale. To understand the origin of different OER activity between Mn_5O_8 and other nanoparticles, electrokinetics and redox peak analysis were conducted. As a result, Mn_5O_8 showed different mechanism (1 electron, 2 proton involved in the reaction before rate determining step) from Mn_3O_4 and Mn_2O_3 (1 electron, 1 proton involved in the reaction before rate determining step), which may cause less active property of Mn_5O_8.

Next, we found that manganese oxide nanoparticles have much higher OER activity than bulk manganese oxide materials. Thus, Mn_5O_8 materials, which has never been investigated as OER catalyst, were further studied to understand why nanoparticles are more active catalyst than bulk manganese oxides. BET analysis and mass activity comparison clearly showed that Mn_5O_8 nanoparticles have much higher catalytic activity than micron sized Mn_5O_8 although surface area effect is considered. In addition, catalytic stability is also enhanced in nanoparticles. These results imply that intrinsic catalytic property can be improved as particle size becomes nanoscale. To find the clue of this intrinsic difference, we conducted EPR analysis to observe

valence behavior of Mn_5O_8 materials. As a result, we found that Mn_5O_8 nanoparticles and micron sized particles have different Mn^{3+} stability during OER catalysis which may cause intrinsic OER property difference between Mn_5O_8 materials.

In this research, we could understand the effect of crystal structure and nano size on OER activity. Understanding those effect is important because they will be a valuable guide to develop outstanding nano sized OER catalyst in neutral condition. Therefore, further research should be conducted to understand completely the effect of crystal structure in nano scale and nano size on the OER activity.

Keywords: Oxygen evolution reaction, electrocatalyst, manganese oxide, nanoparticles, Crystal structure.

Student Number: 2014-21462

Contents

List of Tables

List of Figures

Chapter 1. Introduction

1.1 Upcoming hydrogen energy era

It is important to develop sustainable energy source in the future. Below are the reasons for that. As quality of life of human is improving, energy consumption amount is also increasing. Energy consumption rate over the world is expected to increase from 13.5 TW in 2001 to 27 TW by 2050 and to 43 TW by 2100.[1-3] Conventional energy sources, such as coal and oil, can provide energy requirement of human at present. Conventional energy sources, however, have several limitation. When they are burned, carbon dioxide gas is generated because carbon, which is main component of coal and oil, reacts with oxygen. Because high amount of carbon dioxide can cause global warming,[4, 5] , carbon dioxide emission must be prevented. Furthermore, depletion of conventional energy source can happen in the future unless renewable and sustainable energy source is developed because amount of fossil fuel deposit is limited. Because of the reasons described above, various sustainable energy sources have been developed.

Among the various types of energy sources developed up to date, hydrogen energy gained a lot of attention due to its some advantages. First, hydrogen produces water as by-products when it is used as fuel source, which means no CO2 emisson. Also, hydrogen is non-toxic while conventional energy sources are all toxic and found in dangerous environment. Moreover, hydrogen has much higher energy density (142 kJ/g) than gasoline (46 kJ/g) and natural gas

(47.2 kJ/g).[6] Finally, hydrogen energy can be produced in large scale unlike other non-renewable energy sources.

Nowadays, about 96% of hydrogen gas is produced by natural gas reforming method.[7] However, this method has two critical disadvantages. First, gas reforming reaction is conducted under harsh condition, such as high pressure and temperature condition. Second, gas reforming method produces toxic gas or green-house gases, such as carbon monoxide and carbon dioxide. Because of these reasons, environment-friendly hydrogen production method should be developed.

1.2 Water splitting and necessity of OER catalysts

Because of the reason mentioned in chapter 1.1, water splitting method has received substantial attention as an environment-friendly hydrogen production method due to below reasons. Unlike gas reforming method, water splitting method produces hydrogen in simple, ambient condition. In addition to this, only by-product of water splitting process is oxygen gas.

The concept of water splitting was originated from the oxygen evolving complex, Mn_4CaO_5 cluster, in photosystem II. Thus biological system must be understood to split water efficiently. In the photosystem, there are two separate subunits, photosystem I and photosystem II. In the photosystem II, the water is oxidized into oxygen by Mn_4CaO_5 water oxidation cluster.[8-13] Electrons produced from the water oxidation are excited by visible light at two reaction center, P700 and P680.(Figure 1.1)[14] Excited electrons and surrounding hydrogen ions are combined with the NADP+ (Nicotin amide adenine dinucleotide phosphate), and consequently NADPH, which is reduced form of $NADP^+$, is formed. NADPH, which has reducing power, makes glyceraldehyde 3-phosphate which is essential nutrient in plant.[13] In the meantime, artificial water splitting system has similarity with the natural water splitting system. At the anode, water is oxidized into oxygen molecules, and at the cathode, the protons are reduced into hydrogen by the electrons from the anode.[15, 16] These reactions can be described as below.

Anodic reaction (Oxygen Evolution Reaction, OER)

$O_2 + 4e^- + 4H^+ <--> 2H_2O$ $E_{anodic} = 1.23\ V - 0.059(pH)\ V\ (vs.\ NHE)$ (1)

Cathodic reaction (Hydrogen Evolution Reaction, HER)

$4e^- + 4H^+ <--> 2H_2$ $E_{cathodic} = 0\ V - 0.059(pH)\ V\ (vs.\ NHE)$ (2)

In above equations, thermodynamic potential of water splitting (E^o_{cell} = 1.23V) is observed by subtracting (2) from (1). However, electrolysis doesn't occur by 1.23 V of applied potential. Additional potential is required to begin electrochemical reaction, which is called overpotential(η). Meanwhile, same current must flow at cathode and anode to complete the whole circuit, which means both electrodes(anode and cathode) need overpotential. The overpotential at the cathode and anode is written as η_c and η_a, respectively. Therefore, total applied potential, E_{appl} is described as below:

$$E_{appl} = 1.23V + \eta_c + \eta_a \quad (3)$$

Equation (3) indicates that high overpotential makes the value of whole potential high, resulting in inefficient hydrogen production. However, of two half reactions, anodic half reaction (oxygen evolution reaction, OER) needs higher overpotential than cathodic half reaction, making OER major bottleneck in the overall water splitting process. Reasons of slow OER kinetics are slow transfer rate of four electrons and the high activation energy

barrier for O-O bond formation.[15] Therefore, outstanding OER electrocatalysts must be developed to enhance efficiency of whole water spitting reaction, which means efficient hydrogen production.

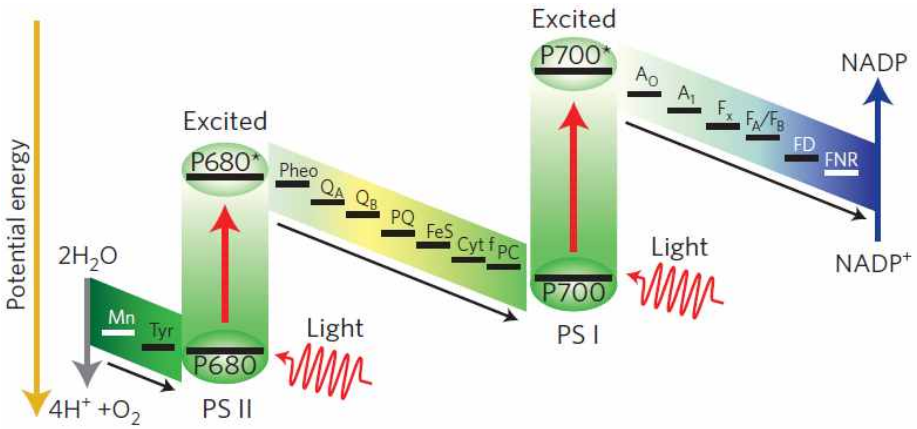

Figure 1.1 Scheme for water splitting in photosystem[14]

1.3 Types of OER catalysts

1.3.1 Noble metal based OER catalysts

Because oxygen evolution reaction is bottleneck of whole water splitting reaction, many scientists have tried to develop efficient OER catalyst to efficiently produce hydrogen. As a result, noble metal based electrocatalysts were developed at first. Typically, ruthenium (Ru), iridium (Ir), and platinum (Pt) were selected to develop efficient OER catalyst in various conditions.[17-19] Due to their unique electronic structure, electrons in transition metal can alternate its oxidation states easily during the water oxidation reaction. As a result, the noble metal based catalysts have higher catalytic activities than other types of catalysts. For example, IrO_x exhibits 1 mA/cm^2 of OER current with the only 200 mV of overpotential (1.43 V vs. RHE) and small Tafel slope value of 40 mV/dec. RuO_2 reaches 1 mA/cm^2 at the applied potential value of 1.36 V vs. RHE and has also small Tafel slope of 40 mV/dec.[20] Trasatti group claimed that moderate metal-oxygen bond strength in RuO_2 and IrO_x caused high OER catalytic activity.[18] Moreover, Norskov and Rossmeisl group theoretically claimed that the high activity of Ruthenium oxide is originated from the difference between the binding energies of O* and OH* which is assumed as rate determining step in the overall water oxidation process.[21] Using DFT calculation, they showed that ruthenium oxide has minimum energy difference among the various transition metal based OER catalyst, supporting their claim.[22-25] Due to the reasons described above, noble metal based oxides gained substantial attention as promising electrocatalysts for

water oxidation.

However, noble metal based catalysts have critical disadvantages. Because noble metals are scarce in earth, price of noble metal is so high (average prices/oz, Ru =$151.96/oz., Pt= $1035.62/oz. and Ir =$476.15/oz.) that it is difficult to use these materials in industrial field. Therefore, noble metal catalysts cannot be used for efficient production of hydrogen energy. Thus, OER catalysts with low-cost and high efficiency must be developed.

1.3.2 Transition metal based OER catalysts

Noble metal based OER catalysts, such as ruthenium oxide and iridium oxide, show outstanding OER activity. However, high price of noble metals makes them difficult to be used in industrial field. Therefore, it is essential to develop effective and inexpensive OER catalysts. In this situation, many researchers tried to develop catalyst which is based on earth-abundant transition metal, such as manganese, cobalt and nickel.[26-32] Meyer group developed Cu based catalysts which exhibits moderate OER activity in alkaline condition.[33] Further, they developed Cu-peptide molecular catalyst whose OER mechanism is well studied.[29] They showed that Cu change its valence from divalent state to trivalent state, and the intermediate tetravalent copper species is generated with the formation of peroxide. Also it was shown that Cu based catalyst has high stability during OER. In this research, they claimed that easy transfer of oxygen atom to water molecule or easy intermolecular oxygen-oxygen coupling are the critical factor for efficient water oxidation. Nocera groups developed cobalt based amorphous OER catalyst(Co-P_i) by facile electrodeposition in aqueous solution containing Co atoms and phosphate anions.[15] Surprisingly, Co-Pi was produced in-situ and showed moderate OER activity(η = 430 mV) in neutral condition. Furthermore, Co-Pi films showed interesting features, self-repairing characteristics. Self-repairing means catalyst films are continuously produced on the original catalyst film during OER.[34] In addition to Co-P_i, Nocera group made nickel based amorphous OER catalyst(Ni-B_i) by facile electrodeposition method.[35] Instead of phosphate buffer containing cobalt ion, they used borate

buffer containing divalent nickel ion to make the films. This Ni-Bi film is also made in situ, and showed moderate OER activity under alkaline condition.[35] Inspired from the active amorphous metal oxide films made by Nocera group, Berlinguette group newly developed amorphous $Fe_{100-y-z}Co_yNi_zO_x$ films.[20] This amorphous films were produced by using photochemical metal-organic deposition method under low temperature condition, which results in homogenous distribution of metal component in the catalyst film. Interestingly, $Fe_{100-y-z}Co_yNi_zO_x$ films showed catalytic stability similar to the iridium oxide catalysts under basic condition. In the meantime, Ni-Fe based layered double hydroxide materials was synthesized on slightly oxidized CNT by Hongjie Dai group.[26] In this research, CNT acted a role as substrate and Ni-Fe LDH acted as OER electrocatalysts. Both materials was used as working electrodes. Surprisingly, this Ni-Fe LDH system showed high catalytic activity similar to the conventional iridium based electrocatalysts. For more systematic comparison of various transition metal oxide electrocatalysts, Jaramilo group developed various kinds of electrocatalysts based on cobalt, iron and nickel via facile electrodeposition method.[27] In this research, overpotential at which current density of 10 mA/cm^2 flow was compared among the various catalysts. As a result, it was shown that these catalysts have moderate overpotential value under alkaline condition.[27]

Meanwhile, another researches focused on the organic-inorganic hybrid material which consists of transition metal and surrounding organic ligands.[28] In this hybrid system, organic ligands helped systematic arrangement of transition metals and stabilize the electronic structure of the metals. By controlling the organic ligands, various transition metal-organic ligand hybrid

materials were developed, such as mononuclear, binuclear and multinuclear complex.[28]

1.4 Manganese based OER catalyst

1.4.1 Mn_4CaO_5 cluster in Photosystem II

As written in previous part, there is a water oxidation complex (WOC) in plant (PS II) consists of the earth-abundant transition metal, Mn and Ca.[8, 10-13, 36] Mn_4CaO_5 cluster, which is the core catalyst of WOC, efficiently oxidize water under neutral conditions with extremely low overpotential value (~160 mV) and a high TOF number (~25,000 $mmol_{O2}$ mol^{-1}_{Mn} s^{-1}). These outstanding catalytic property of WOC cannot be achieved with the any other artificial electrocatalyts.[11] Recently, some researcher studied structure of the PSII using X-ray analysis, identifying that Mn_4CaO_5 cluster is stabilized by a surrounding peptide ligand.[37] Based on this results, they claimed that four Mn atoms are oxo-bridged in asymmetric way and oxidation state of four Mn atoms continuously change during catalytic reaction, which is so-called Kok cycle. Also, it was suggested that oxygen bond formation occurs at specific sites in the Mn_4CaO_5 cluster.[11, 13]

1.4.2 Artificial Mn based OER catalysts and their limits

Outstanding catalytic property of cubical Mn_4CaO_5 cluster have inspired many researcher to develop Mn based electrocatalyst.[38-43] Because manganese is the only redox active metal which can change its valence state easily and rapidly from lower oxidation states to higher oxidation states (2+ ~ 7+) in the cluster, various manganese based compounds has been developed for water splitting catalysts. Especially, researchers have focused on the asymmetric geometry and mixed valent (III/IV) states of Mn atoms in the WOC.[38-43] For example, the geometry of oxo-bridged Mn atoms has been synthetically controlled by designed organic ligands. $[Mn_4O_4L_6]^+$(L =$(MeOPh)_2PO_2$) or $[Mn_4O_4L_6]^+$-Nafion system have been recently demonstrated as efficient water oxidation catalysts.[38, 39] Especially, Agapie group developed $[Mn_3CaO_4]^{6+}$ core which is structure very similar to the manganese calcium cluster in WOC of PS II.[40] This was the first work that realize the local Mn geometry of the WOC. Further, they made $Mn_3M(\mu_4\text{-}O)(\mu_2\text{-}O)$(M = Ca^{2+}, Sr^{2+}, Na^+, Zn^{2+}, Y^{3+}) complex to identify the role of redox inactive metals during water oxidation reaction in WOC.[41] By electrochemical analysis, they found that redox potential of manganese can change by redox inactive metals (M). As a result, they concluded that calcium ions in the cluster of WOC might help to change the redox potential of Mn atoms in the WOC, and consequently enhances the reaction rate.

On the other hand, various crystalline manganese oxide polymorphs and amorphous MnO_x have been developed as more practical water oxidation catalysts. The Driess group produced active MnO_x nanoparticles from inactive

MnO nanoparticles using ceric ammonium nitrate (CAN) as the oxidant, and they showed that active MnO_x is more efficient than Mn_3O_4 but less efficient than Mn_2O_3.[44, 45] Kuo et al. fabricated a robust mesoporous Mn_2O_3 catalyst that has a high surface area and Mn^{3+} content.[46] The Nakamura group enhanced the OER properties of MnO_2 by stabilizing Mn^{3+} on the surface of MnO_2.[47, 48] Kurz group developed $CaMn_2O_4$-$4H_2O$ as an improved water oxidation catalyst by mimicking the natural Mn_4CaO_5 cluster.[42] Dismukes group developed λ-MnO_2 with $[Mn_4O_4]$ core units in the WOC by removing Li ions from $LiMn_2O_4$ Li-ion battery cathode material.[49] Dau group developed new electrodeposition method which can present active MnO_x film.[50] This new film shows much higher activity than conventionally electrodeposited films. Using EXAFS and XANES analysis, they found that the newly developed electrodeposited amorphous MnO_x films have mixed valency (III/IV) and disordered Mn geometry which are recognized as important properties of the WOC in nature. Jaramillo group found that the active manganese oxide catalysts have mixed valency state of Mn(III/IV) that is similar with the valency state in the Mn_4CaO_5 cluster in photosystem II.[51] In addition to these materials, there are so many manganese oxide materials developed to date.

Therefore, some researchers tried to synthesize various kinds of manganese oxide to compare their activity and structural difference for identification of OER activity enhancement factor, which helps to design more efficient OER catalyst. Kurz group synthesized 14 types of manganese oxide, including crystalline material(α-Mn_2O_3, Mn_3O_4(spinel), $LiMn_2O_4$(spinel), $CaMn_2O_4$(marokite), MnO), tunneled material(β-MnO_2, R-MnO_2,

Cryptomelane(α-MnO_2 with small amount of potassium), α-MnO_2, Todorokite) and layered material(Ca-birnessite(δ-MnO_2), K-birnessite(δ-MnO_2), Vernadite(δ-MnO_2).[52] They compared the chemical water oxidation activity of these materials. In the case of normalization with manganese ion number, most crystalline material showed no OER activity. Most efficient catalyst was Ca-birnessite with layered strucutre. On the other hand, Dismukes group compared the photochemical water oxidation activity of 8 manganese oxides normalizing with surface area.[53] In their research, Mn_2O_3 showed outstanding activity and Mn_3O_4 followed next. Suib group compared both photochemical and chemical water oxidation activity of manganese oxides and suggested following property order: amorphous manganese oxide > α-MnO_2 > K-birnessite(δ-MnO_2).[54] Meng et al. compared electrochemical water oxidation property of amorphous MnO_x and various MnO_2 polymorphs.[55] They claimed that α-MnO_2 is the most efficient OER catalyst among the other MnO_2 phases.

Based on above results(summarized in Table 1.1), each group claimed that following factors enhanced OER activity of manganese oxide.

- Ions or water molecule inside crystal structure
- Low degree of order in crystal structure (Degree of amorphous is important)
- Trivalent manganese species(Mn^{3+})
- Defect in material
- Charge transfer resistance

From these claims, we concluded that crystal structure is the critical factor deciding OER activity of bulk manganese oxide materials. Based on this conclusion, our group synthesized new material, $Mn_3(PO_4)_2$-$3H_2O$, and

confirmed that asymmetric crystal structure of $Mn_3(PO_4)_2$-$3H_2O$ enhanced OER activity.[56] Further, we identified the effect of trivalent manganese species on OER activity of $Li_xMnP_2O_7$ ($1<x<2$) by changing manganese valency via delithiation from $Li_2MnP_2O_7$.[57]

While manganese oxides are very attractive OER catalysts, conventional manganese oxides have a critical disadvantage; low activity and stability in neutral pH. Neutral pH is essentially required condition for realization of artificial leaf device because component of artificial leaf is unstable in acid and basic condition. Therefore, it is essential to develop manganese oxide catalyst which is active in neutral condition. Previously, our group focused on the nanoparticle for solving the low activity issue of manganese oxide and synthesized sub 10 nm sized MnO nanoparticles.[58] After then, we conducted facile surface treatment, resulting in partially oxidized MnO nanoparticles. As shown in Table 1.2, this material showed the highest OER activity in neutral condition among the various manganese oxide electrocatalysts reported to date. In this situation, it is required to study applicability of various claims described above on the manganese oxide nanoparticles. Also, we have to understand what makes nanoparticles much more active catalyst than bulk manganese oxides. These study will be useful for developing highly efficient OER catalyst in neutral condition.

Table 1.1 Summary of various manganese oxide OER activity comparison research.

Catalyst	Best(100%)	Good(>70%)	Moderate(>40%)	Bad(>10%)	Inactive
MnO					K(1), K(2)
Mn_3O_4				D	K(1), K(2)
Mn_2O_3	D	K(3)	K(2)	K(1)	
$CaMn_2O_4$	K(2)			K(1), S(1)	
β-MnO_2		S(3)		K(1), K(2), K(3)	D
α-MnO_2 (K^+)	S(3)	S(1), S(2)	K(1), K(2)		D
δ-MnO_2 (Ca^{2+})	K(1), K(3)		K(2)		
δ-MnO_2 (K^+)		K(2)	K(1)	S(1), S(2), S(3)	D
AMO	S(1), S(2)	S(3)			

Table 1.2 Summary of OER activity of various manganese oxide in neutral pH

Increasing activity

Catalyst	Overpotential at neutral pH
Partially oxidized MnO NPs	440 mV (@ 1mAcm^2)
δ-MnO_2(Ca-birnessite)	480 mV (@ 1mAcm^2)
Mn_2O_3	500 mV (@ 1mAcm^2)
β-MnO_2	560 mV (@ 1mAcm^2)
MnO_x-1	600 mV (@ 1mAcm^2)
MnO_x-2	633 mV (@ 1mAcm^2)
δ-MnO_2(K-birnessite)	840 mV (@ 1mA/cm^2)
$LiMnP_2O_7$	680 mV (@ 0.5 mA/cm^2)
$Mn_3(PO_4)_2 \cdot 3H_2O$	673 mV (@ 0.3 mA/cm^2)
$Li_2MnP_2O_7$	680 mV (@ 0.2 mA/cm^2)

Chapter 2. Experimental Procedures

2.1 Synthesis of various Mn oxide materials

2.1.1 Materials

Manganese acetate dehydrate ($Mn(CH_3COO)_3$-$2H_2O$, 97%), Decanol ($CH_3(CH_2)_9OH$, >99%), Octadecene ($CH_3(CH_2)_{15}CH=CH_2$, 90%) Ammonia hydroxide solution (ACS reagent, 28.0-30.0% NH_3 basis), Toluene ($C_6H_5CH_3$, >99%), Manganese chloride tetrahydrate ($MnCl_2$-$4H_2O$, 98%), Myristic acid ($CH_3(CH_2)_{12}COOH$, >99%), Nafion 117 solution was purchased from Sigma Aldrich and used without additional purification. Sodium oleate (TCI, 95%), 1-hexadecene (TCI, > 90%), Ethyl alcohol (Daejung, 99%), isopropanol (Acros, 99.5%) and n-hexane (Daejung, > 95%) was used as received without further purification. Neutralized Nafion was prepared by adjusting pH of Nafion 117 solution to 7 with 0.1 M NaOH solution. Fluorine doped Tin Oxide coated glass (FTO, TEC-8) which has 15 Ω sq-1 surface resistivity was obtained from Pilington Company.

2.1.2 Synthesis of MnO nanoparticles

MnO nanoparticles were prepared using conventional nanoparticle synthesis method, hot injection and heat up. For MnO nanoparticles whose purpose is to compare various manganese oxide nanoparticles, hot injection method was

used. For MnO nanoparticles whose purpose is to compare Mn_5O_8 materials, heat up method was used.

First, Hot injection method is as follows. In one flask, 1 mmol of manganese acetate dehydrate(0.2764 g) and 2 mmol of myristic acid(0.4567 g) were mixed with 20 ml of 1-octadecene.(solution with manganese precursor) Simultaneously, 1.83 ml of decanol and 3.072 ml of 1-octadecene is mixed in another flask.(alcohol solution) Both flask is heated up to 110° C with stirring under degassed atmosphere. The temperature is kept for 1 hour. After then, argon gas is put into both flask. Then, solution with manganese precursor is heated up to 295° C under argon atmosphere. Right after the temperature reached to 295° C, 1.2 ml of alcohol solution is injected to mixture with manganese precursor to make supersaturated solution by relatively cold solution and micelle destruction. After then, the temperature of mixture solution is adjusted to 285° C, whose temperature is kept for 1 hour. In this process, the color of solution transformed from transparent brown to opaque dark brown, which means growth of MnO nanoparticles.

Solution of MnO NPs for comparing Mn_5O_8 materials was obtained by modifying heat up method reported previously.[59] The solution of Mn^{2+} oleate, myristic acid and 1-hexadecene was heated to 60 °C until Mn^{2+} oleate and myristic acid were completely dissolved with vigorous stirring. The solution was heated to 100 °C and degassed for 30 minutes. After then, argon gas was put into degassed atmosphere. This solution was heated to 285 °C at a rate of 5 °Cmin^{-1} to burst nucleation by thermal decomposition of Mn oleate precursor. After then, temperature of the solution was kept for 2 hours to give enough time for nanoparticles to grow.

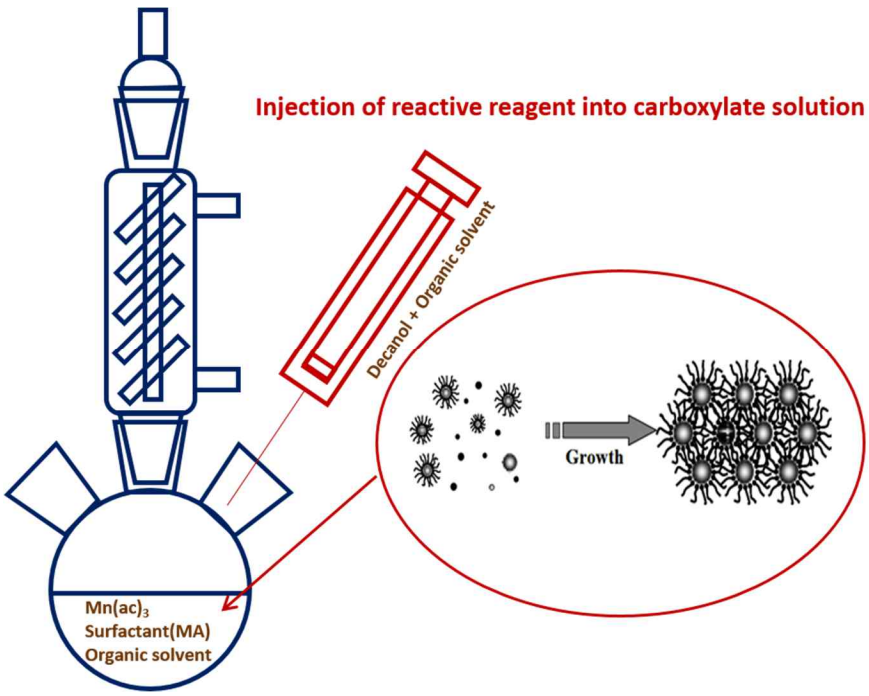

Figure 2.1 Scheme of hot injection method for nanoparticle synthesis

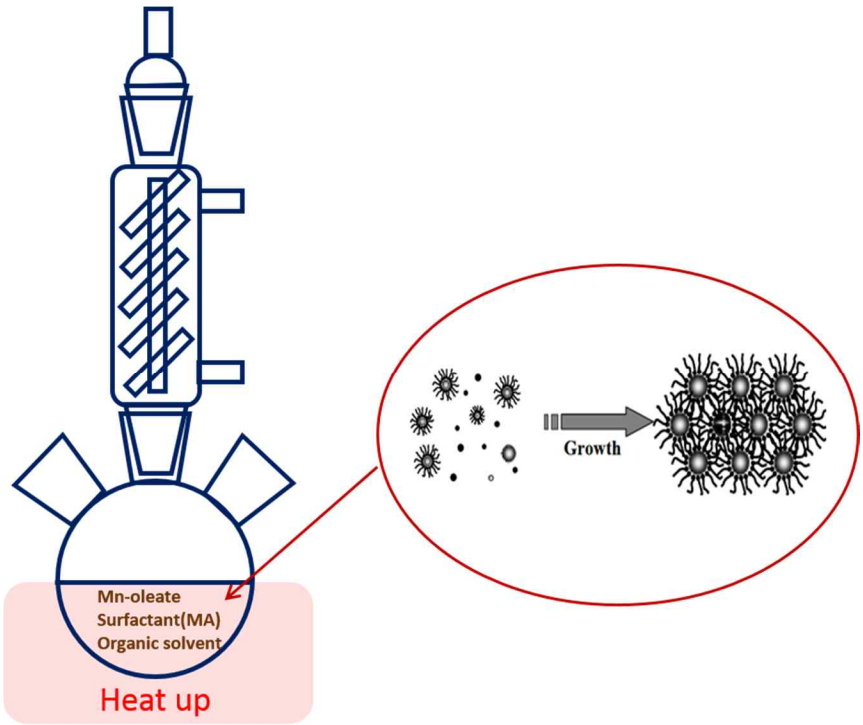

Figure 2.2 Scheme of heat up method for nanoparticle sysnthesis

2.1.3 Synthesis of Mn_3O_4, Mn_2O_3 and Mn_5O_8 nanoparticles

As-prepared solution of MnO NPs was washed with acetone and toluene three times to get rid of solvent and supernatant surfactant. To obtain powder of manganese oxide NPs, washed MnO NPs was freeze-dried for 24 hours. To obtain film of manganese oxide NPs, hexane solution containing washed MnO NPs was spin coated onto the FTO glass (1 cm by 1.5 cm). Prepared MnO NPs (powder or film on FTO glass) were annealed under specific condition to transform its phase into Mn_3O_4, Mn_2O_3 and Mn_5O_8. To obtain Mn_3O_4, MnO NPs were annealed at 250 °C for 1 hour under air atmosphere. Annealing time didn't matter if it is longer than 1 hour. To obtain Mn_2O_3, MnO NPs were annealed at 500 °C for 20 hour under air atmosphere. If annealing time is shorter than 20 hour, there is possibility of Mn_5O_8/Mn_2O_3 mixture phase. To obtain Mn_5O_8, MnO NPs heated up 1°C/min until the temperature reached 375 °C under oxygen flow of 500 cc/min. The temperature was kept for 15 hours followed by natural cooling.

2.1.4 Synthesis of micron sized Mn_5O_8 particles

Micron-sized Mn_5O_8 was synthesized by modifying previous method. First, γ-MnOOH precursor was prepared using previously reported hydrothermal method. After then, it was annealed at 1°C/min until the temperature reached 400 °C under nitrogen flow of 500 cc/min and the temperature was kept for 2 hours to obtain Mn_3O_4 rod. This material was annealed again at 4°C/min until the temperature reached 410 °C under air atmosphere and kept for 12 hours.

As a result, micron-sized Mn_5O_8 was obtained. All the materials were obtained as powder.

2.2 Characterization

2.2.1 Powder X-ray Diffraction (PXRD)

Phase was identified with Powder X-ray diffraction(PXRD) data collected on a Bruker D8 ADVANCE X-ray diffractometer with Cu K α1 radiation (wavelength(λ) : 1.5418 Å). The sample was prepared by drying manganese oxide nanoparticles by lyophilizer for 1 day. Obtained powder of manganese oxide materials was loaded on a Si holder, retrofitted in X-ray diffractometer. XRD patterns of manganese oxide materials were recorded in a range of 15~65° with a step of 0.01° and a velocity of 1°/min. XRD patterns of precursor of micron sized Mn_5O_8 were recorded in a range of 15~65° with a step of 0.02° and a velocity of 2.5°/min. Obtained XRD patterns were compared with previously reported JCPDS cards.

2.2.2 Scanning Electron Microscopy (SEM)

The morphology of manganese oxide materials on FTO glass was characterized with a high resolution scanning electron microscope (Supra 55VP, Carl Zeiss, Germany). For the analysis of MnO NPs, hexane solution containing MnO NPs was spin coated onto FTO glass. SEM sample for Mn_3O_4, Mn_2O_3, Mn_5O_8 NPs were prepared using previously mentioned method as film state. For the analysis of micron-sized Mn_5O_8 and its precursor materials, aqueous solution containing them was dropped onto the FTO glass.

2.2.3 Transmission Electron Microscopy (TEM)

Transmission electron microscopy (TEM) images and selected area electron diffraction (SAED) patterns were obtained using a high resolution transmission electron microscope (JEM-2100F, JEOL, Japan) with an acceleration voltage of 200 kV. TEM samples were prepared via two different ways. For the MnO nanoparticles, hexane solution containing MnO nanoparticles was dropped on the TEM grid and dried in an oven. For the Mn_3O_4, Mn_5O_8, Mn_2O_3 nanoparticles, aqueous solution containing powder of manganese oxide materials was dropped on the TEM grid and dried in an oven. For the stability test of Mn_5O_8 nanoparticles, the TEM samples were collected from FTO glass right after bulk electrolysis, and dispersed in water by sonication about 10 min. The solution was dropped on the TEM grid and dried in an oven.

2.2.4 Brunauer-Emmett-Teller (BET) method

Brunauer-Emmett-Teller (BET) analysis was conducted for surface area comparison between Mn_5O_8 nanoparticles and micron sized Mn_5O_8 particles. Powders of Mn_5O_8 nanoparticles (83.5 mg) and micron sized Mn_5O_8 (103.3 mg) were loaded to BET analyzer (Physisorption Analyzer, micromeritics, USA) under N_2 adsorption environment.

2.3 Electrochemical analysis

All electrochemical experiments were done under a three-electrode electrochemical cell system. We used BASi Ag/AgCl/3M NaCl electrode and a Pt foil(2 cm × 2 cm × 0.1 mm, 99.997 % purity, Alfa Aesar) as a reference and counter electrode, respectively. Electrochemical tests were carried out under ambient temperature using a potentiostat system(CHI 600D, CH Instruments). Electrolyte was 0.3 M sodium phosphate buffer whose pH is 7.8. All the data were iR-compensated with the resistance which was recorded before measurements. Electrode potential was converted to the NHE scale, using the following equation: E(NHE) = E(Ag/AgCl) + 0.197 V - iR

2.3.1 Cyclic Voltammetry (CV)

Cyclic voltammetry (CV) is a type of potentiodynamic electrochemical measurement. In a cyclic voltammetry experiment the working electrode potential is ramped linearly versus time. Unlike in linear sweep voltammetry, after the set potential is reached in a CV experiment, the working electrode's potential is ramped in the opposite direction to return to the initial potential. These cycles of ramps in potential may be repeated as many times as desired. The current at the working electrode is plotted versus the applied voltage (i.e., the working electrode's potential) to give the cyclic voltammogram trace. In this research, voltage range was set from 0 to 1.3 V (vs. Ag/AgCl). All CV measurements were conducted with scan rate of 0.01 V/s except long cycle CV measurement (scan rate: 0.1 V/s).

2.3.2 Bulk Electrolysis (BE)

Bulk electrolysis is also known as potentiostatic coulometry or controlled potential coulometry. The experiment generally employs a three electrode system controlled by a potentiostat. In the experiment the working electrode is held at a constant potential (volts) and current (amps) is monitored over time. In this research bulk electrolysis was used to compare the electrochemical stability of Mn_5O_8 nanoparticles and micron sized particles. 1.2 V (vs. Ag/AgCl) was applied for 5000 seconds.

2.3.3 Faradaic efficiency measurement

To confirm that recorded current is generated from oxygen evolution, faradaic efficiency measurement was conducted. Before bulk electrolysis, the designed electrochemical cell was purged with inert gas (99.999% Ar) for 1 h, and the fluorescence sensor was located in the upper part of the cell. During electrolysis, produced oxygen molecules were measured by a fluorescence-based O_2 sensor. Electrolysis was performed at the applied potential of 1.2 V vs. Ag/AgCl for 2500 sec. The theoretical yield of oxygen during electrolysis was calculated from the total charge passed during the electrolysis.

2.3.4 Preparation of working electrode

Working electrode of manganese oxide nanoparticles for cyclic voltammetry (CV) and bulk electrolysis (BE) was prepared using above mentioned method

for film. To compare mass activity of Mn_5O_8 materials, loaded amount of Mn_5O_8 NPs (32.265 ug) on FTO glass was measured with ultramicro balance (Satorius). For the preparation of micron sized Mn_5O_8 working electrode, obtained powder (7 mg), deionized water (1 ml) and neutralized Nafion solution (200 ul) were mixed together with tip sonicator for 15 minutes and 5.53 ul (containing 32.265 ug of micron sized Mn_5O_8 rod) of the solution was dropped onto the FTO electrode. For conductivity enhancement, we made micron sized Mn_5O_8 working electrode using another recipe. Obtained powder (6.7 mg), Vulcan C (4.5 mg), isopropanol (IPA, 250 ul), deionized water (750 ul) and neutralized Nafion solution (20 ul) were mixed together with tip sonicator for 15 minutes and 4.9 ul(containing 32.265 ug of micron sized Mn_5O_8) was dropped onto the FTO electrode. For enhancement of bulk electrolysis stability of Mn_5O_8 NPs, 20 ul of mixture solution of neutralized Nafion solution (100 ul) and IPA (1900 ul) was dropped onto the Mn_5O_8 NPs film on FTO glass.

2.4 Electron Paramagnetic Resonance (EPR) analysis

All EPR measurements were carried out at KBSI, Seoul, Korea. Electron paramagnetic resonance (EPR) was performed using a Bruker EMX/Plus spectrometer equipped with a dual mode cavity (ER 4116DM). Low temperatures were achieved and controlled using a liquid He quartz cryostat (Oxford Instruments ESR900) with a temperature and gas flow controller (Oxford Instruments ITC503). The experimental conditions are as follows. Microwave frequency 9.64 GHz (perpendicular mode), 9.4 GHz (parallel mode), modulation amplitude 10G, modulation frequency 100 kHz microwave power 0.94mW (perpendicular mode), 5.0 mW (parallel mode) temperature 5.7K. 10 scans were added for each spectrum. EPR samples were prepared as follows. Catalyst powder of Mn_5O_8 materials (6.7 mg), Vulcan C (4.5 mg), IPA (250 ul), deionized water (750 ul) and neutralized Nafion solution (20 ul) were mixed together with tip sonicator for 15 minutes. 20 ul of the obtained ink was loaded onto FTO glass (1.5 cm by 2.5 cm) and dried in an oven. For the as-prepared samples, as-made Mn_5O_8 materials on FTO glass were transferred to an EPR tube by blade with 180 ul of pyrophosphate aqueous solution (PP, 20 mM) and 20 ul of glycerol. The EPR tube was frozen and stored at 77 K in liquid nitrogen immediately. For the samples after OER, 1.25 V (vs. Ag/AgCl) was applied to Mn_5O_8 sample for 1000 seconds in same electrolyte mentioned above. After then, Mn_5O_8 materials were transferred to an EPR tube by blade with 180 ul of PP solution (20 mM) and 20 ul of glycerol as promptly as possible. Likewise, the EPR tube was frozen and stored at 77 K in liquid nitrogen immediately.

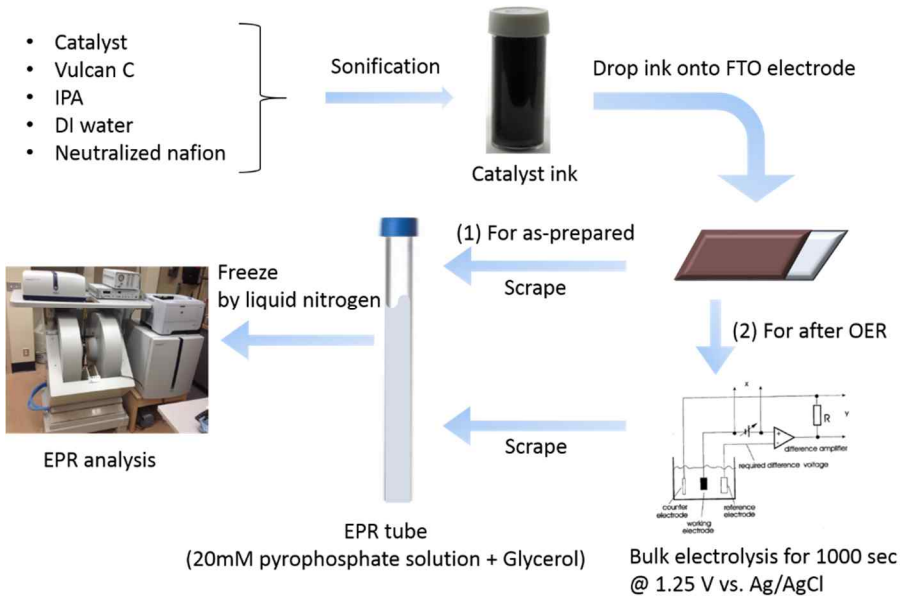

Figure 2.3 Scheme of EPR sample preparation process

Chapter 3. Results and Discussion

3.1 Characterization of Mn oxide nanoparticles

3.1.1 Effect of annealing on the crystal structure of Mn oxide nanoparticles

To investigate the effect of crystal structure on the OER catalytic property of manganese oxide nanoparticles, we developed various manganese oxide phase using MnO nanoparticles as precursor material. At first, we synthesized about 10 nm sized MnO nanoparticles using conventional hot injection method. Its phase was identified by powder X-ray diffraction analysis (figure 3.3, black line). Also, morphology of sphere nanoparticles was confirmed by SEM image (figure 3.4). After then, we transformed its phase to another manganese oxide phase by annealing under specific condition. To find the specific condition in which each manganese oxide phase is stable, we referred to phase diagram of bulk manganese oxide materials (Mn_3O_4, Mn_2O_3, MnO_2) because there is no phase diagram for manganese oxide nanoparticles. As shown in figure 3.1, MnO_2 is stable under low temperature and oxygen rich atmosphere and Mn_2O_3 is stable under medium temperature and oxygen moderate atmosphere and Mn_3O_4 is stable under high temperature and oxygen deficient atmosphere. This indicates that bulk manganese oxide materials tend to have a higher manganese valence(more oxidized phase) when they exist under oxygen-rich and low temperature atmosphere.

Thus, we tried to anneal the MnO nanoparticles considering the stable thermodynamic condition for MnO_2, Mn_2O_3, Mn_3O_4 phase. However, there was a substantial difference between the phase diagram of bulk manganese oxide and the result we got. In our system, Mn_3O_4 was obtained at low temperature(250° C), which is totally mismatched with the phase diagram of bulk manganese oxides(MnO_2 phase is stable at 250° C under ambient atmosphere). We think this phenomenon might happen because of two reasons as follows. First, temperature of 250° C or annealing time at the temperature are not enough to provide required activation energy for transformation of MnO into Mn_2O_3 or Mn_3O_4. Second, MnO nanoparticles are easily oxidized due to its high surface area and nature which is different from bulk materials. Because of the reasons described above, we couldn't obtain MnO_2 phase by annealing process. We tried to various annealing condition, but another phase (Mn_2O_3 or Mn_5O_8 phase) was obtained instead of MnO_2. Synthesis conditions for various manganese oxide are summarized in figure 3.2. Surprisingly, Mn_5O_8 phase which is not described in the phase diagram of manganese oxide was obtained in the annealing process. However, pure Mn_5O_8 was difficult to obtain in the air atmosphere because of its meta stable nature. Thus, we tried oxygen atmosphere annealing for pure Mn_5O_8 nanoparticles and succeeded.

All the phase of manganese oxide nanoparticles was confirmed using powder X-ray diffraction which is shown in figure 3.3. Interestingly, degree of noise was different among manganese oxide materials. For Mn_3O_4 and Mn_5O_8 which was obtained by phase transformation without sintering, degree of noise increased, indicating decrease of crystallinity. However, Mn_2O_3 phase showed very sharp peak feature without noise. That's because Mn_2O_3 was

sintered under high temperature annealing process(500° C, 20hr).

Morphology of various manganese oxide nanoparticles are observed by SEM image. As shown in figure 3.5, Mn_3O_4 and Mn_5O_8 nanoparticles maintained the nanoparticle morphology of precursor material (MnO nanoparticle). Unfortunately, Mn_2O_3 was obtained with a little bit of sintering, which is matched result with the XRD data. However, although Mn_2O_3 failed to maintain the original morphology of MnO nanoparticles, a part of Mn_2O_3 showed nanoparticle morphology, which is totally different from bulk material.

Therefore, we controlled the concentration of precursor material to obtain Mn_2O_3 nanoparticles without sintering. Surprisingly, as shown in figure 3.6, nanoparticles was obtained without sintering under same condition(500° C, 20hr) when we decreased the concentration of MnO film into one fourth. This result shows that concentration of nanoparticles affect the degree of sintering. However, phase of nanoparticle film shown in figure 3.6(a) cannot be identified because its film thickness is so thin that XRD peak of FTO substrate covered all the peaks of manganese oxide materials.

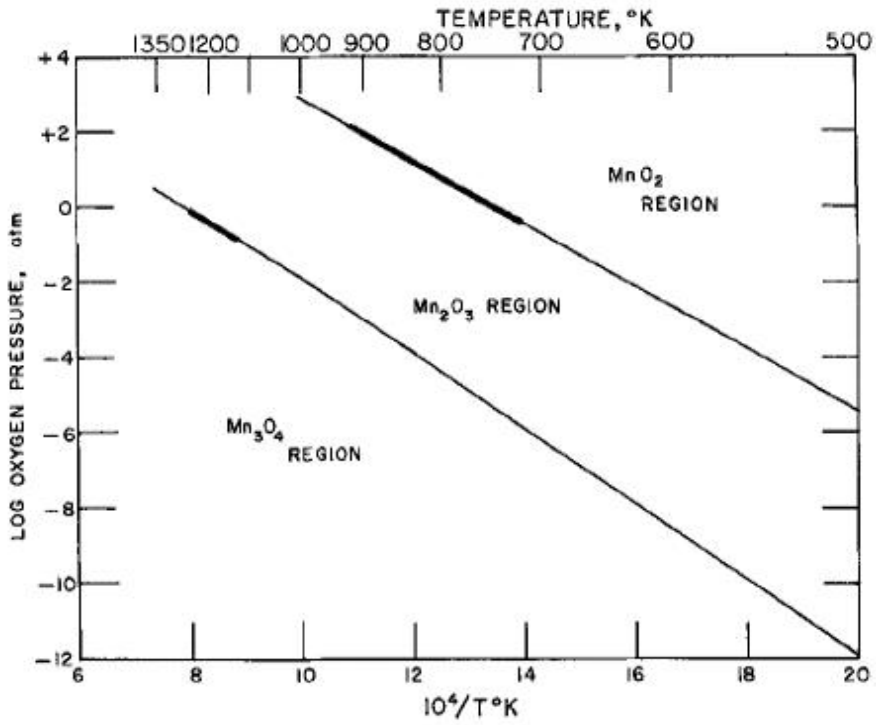

Figure 3.1 Phase diagram of bulk manganese oxide materials

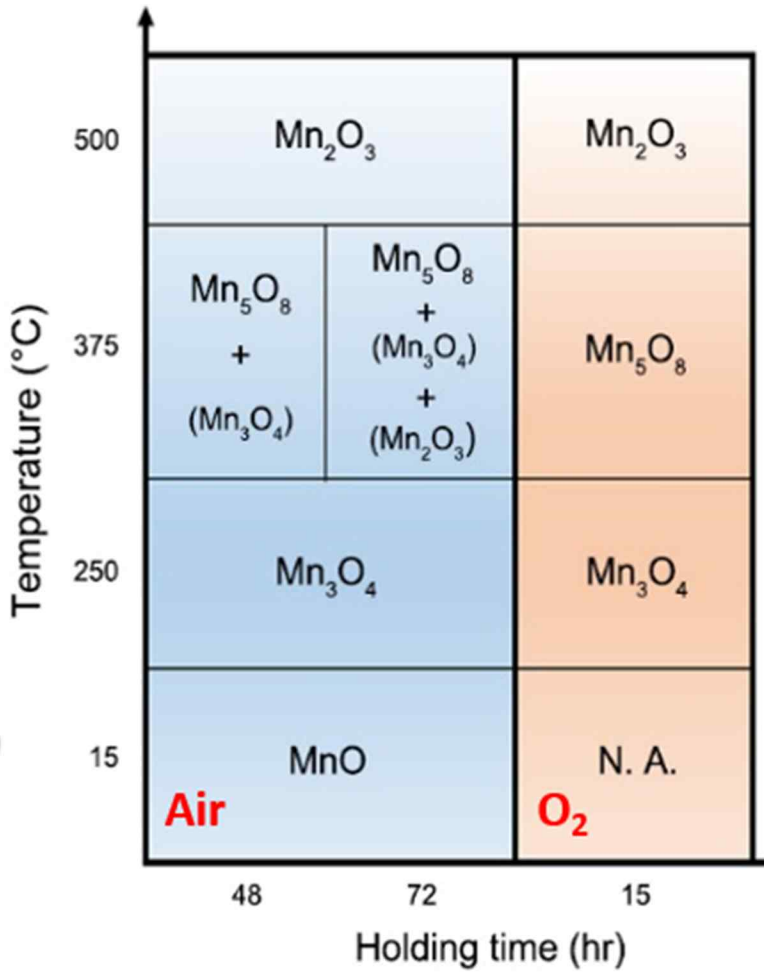

Figure 3.2 Synthesis condition of various manganese oxides (blue region: air atmosphere, red region: oxygen atmosphere)

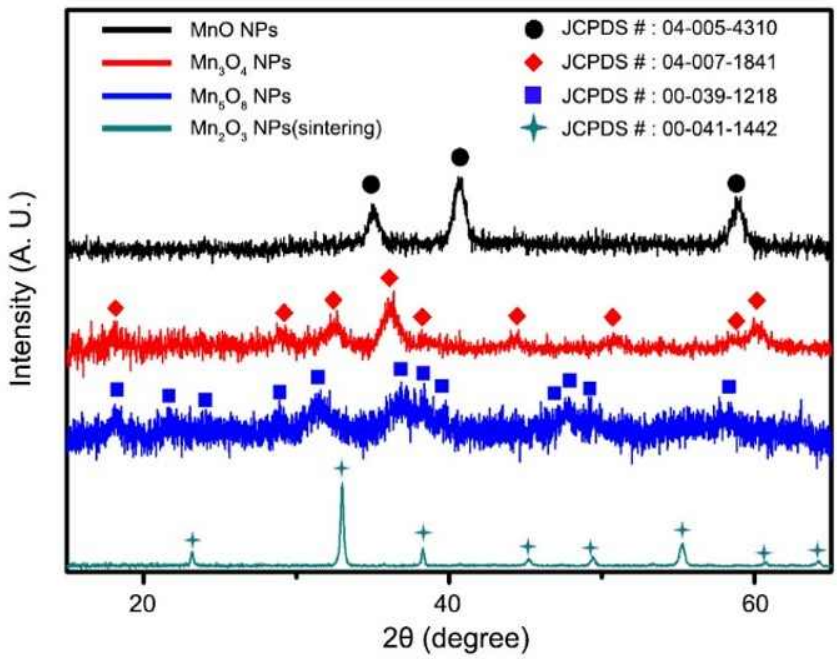

Figure 3.3 Powder X-ray diffraction results of various manganese oxides made from MnO nanoparticles (NPs).

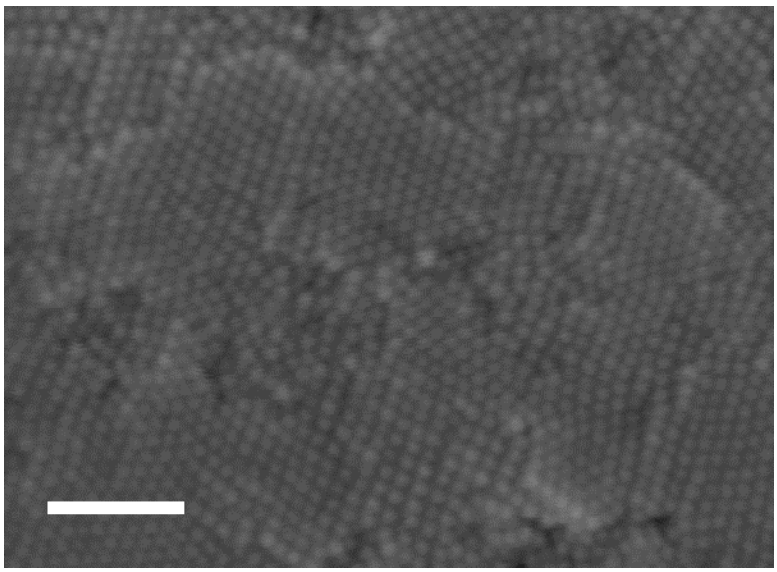

Figure 3.4 Morphology of as-prepared MnO nanoparticles. Scale bar: 100 nm

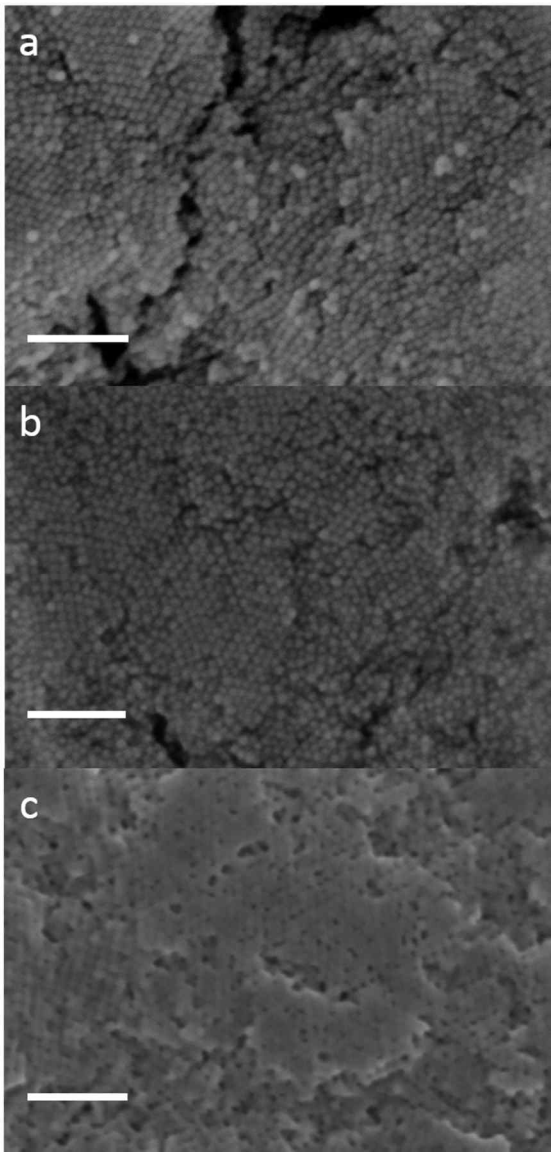

Figure 3.5 Morphology of manganese oxide nanoparticles. (a) Mn_3O_4 NPs; (b) Mn_5O_8 NPs; (c) Mn_2O_3 NPs(a little bit sintered) Scale bar: 100 nm

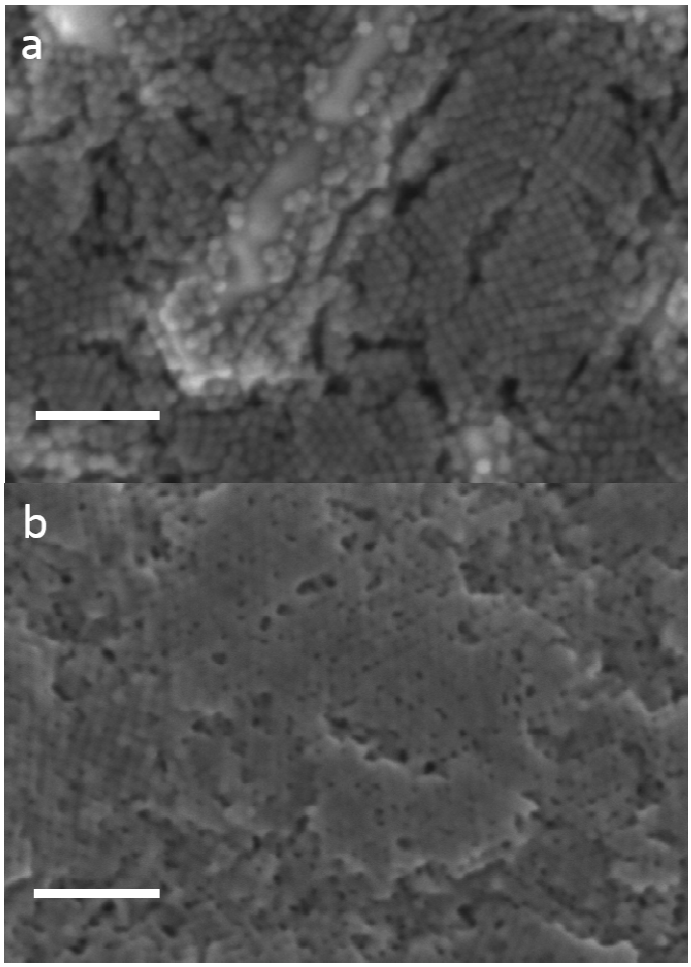

Figure 3.6 SEM image of annealed nanoparticles at 500°C for 20 hours. (a) Low concentration and (b) High concentration of precursor nanoparticles. Scale bar: 100 nm

3.2 Effect of crystal structure on the catalytic property

3.2.1 Water oxidation property of Mn oxide nanoparticles

The water oxidation activity of various manganese oxide nanoparticles was evaluated using cyclic voltammetry (CV). Compared materials are Mn_3O_4, Mn_5O_8 and Mn_2O_3 nanoparticles. Previously reported partially oxidized MnO nanoparticles were also compared instead of as-prepared MnO nanoparticles because as-prepared MnO have poor activity because of its surrounding organic ligand which hinders electron transfer between nanoparticles and electrolyte. The manganese oxide nanoparticles were prepared on a fluorine-doped tin oxide (FTO) glass substrate using spin coating. (See the experimental procedures for the cell preparation details.) The evaluation for OER activity was performed at pH 7.8 and in a 0.3 M sodium phosphate buffer solution. Catalytic properties of manganese oxide nanoparticles under near neutral conditions are displayed in figure 3.7. As shown in figure 3.7, Mn_3O_4 and Mn_2O_3 showed similar level of OER activity with partially oxidized MnO nanoparticles, whose OER activity is best among the various manganese based OER electrocatalysts under neutral condition to date. On the other hand, Mn_5O_8 nanoparticles showed moderate level of OER activity. To compare precisely the OER activity of manganese oxide nanoparticles, we measured each samples four times and summarized the result into the figure 3.8. From these results, we confirmed that effect of crystal structure on OER activity is reduced in nano sized materials unlike bulk materials. Further, the claim, Mn^{3+} species is related with higher OER activity, can be applicable to

nanoparticles among the various claims on OER property enhancement factor which was described in introduction part while the claim, degree of amorphous is important for OER activity, is not. To develop more efficient nanoparticle based OER catalyst, more hypotheses must be verified in nano sized catalysts, such as effect of defect, charge transfer resistance, etc.)

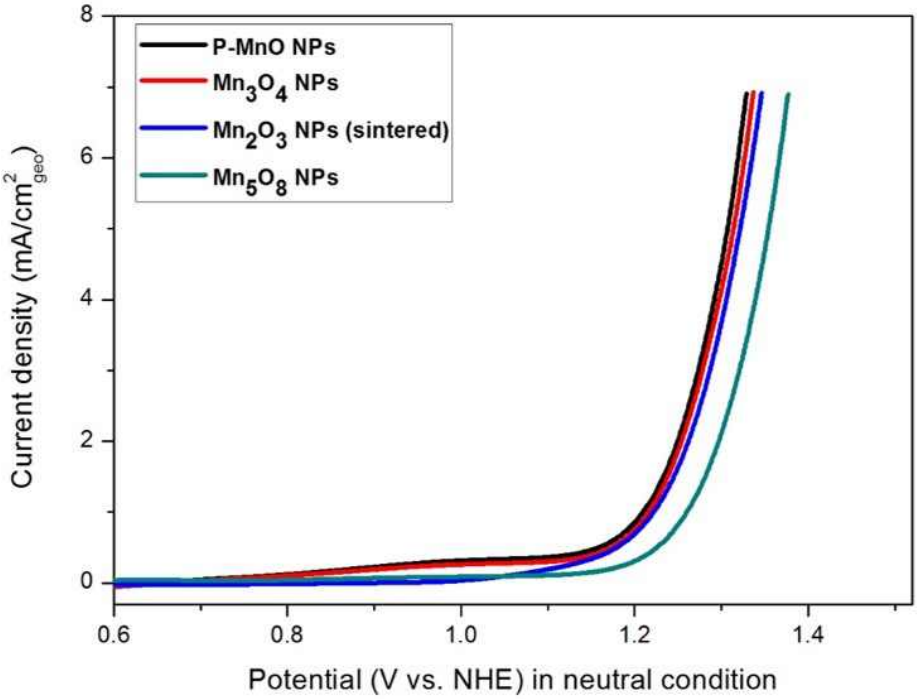

Figure 3.7 Polarization curves of manganese oxide nanoparticles at pH 7.8 in a 0.3 M phosphate buffer solution. Scan rate: 0.01 V/s

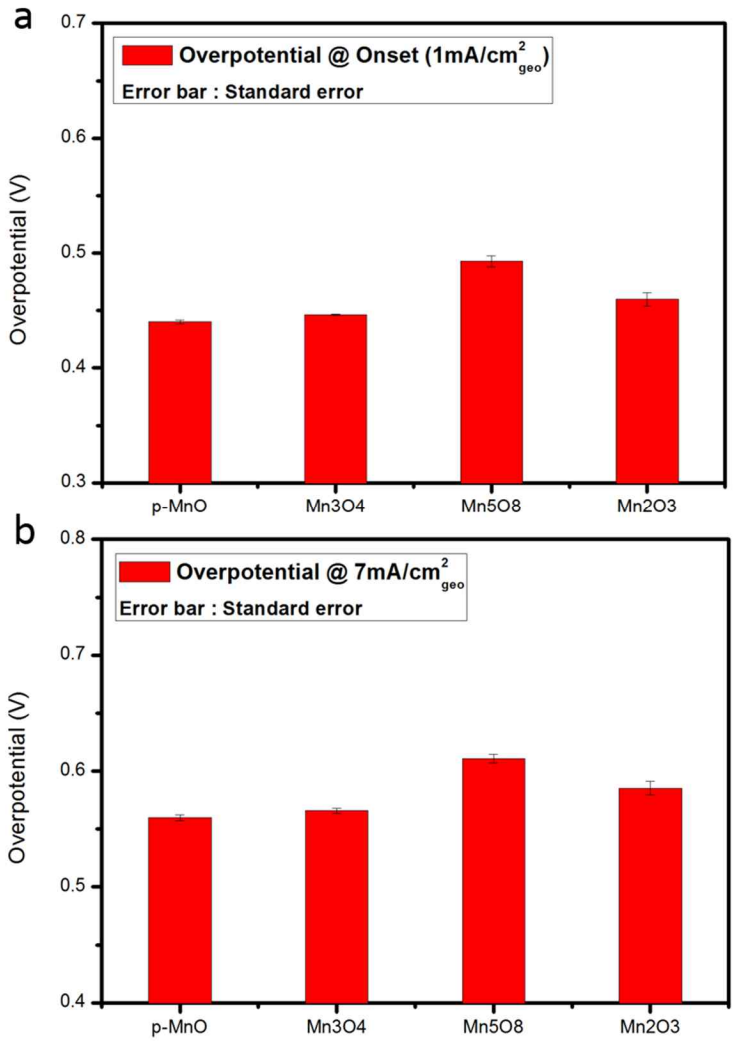

Figure 3.8 Comparison of catalytic property of manganese oxide nanoparticles.

3.2.2 Electrokinetics study and redox peak analysis

To understand the origin of activity difference depending on the phase of manganese oxide nanoparticles, we tried to study OER mechanism of Mn_3O_4, Mn_2O_3 and Mn_5O_8. We excluded partially oxidized MnO nanoparticles because their phase is MnO/Mn_3O_4 mixture, strictly speaking. Among the various ways to understand the mechanism of catalysis, electrokinetics and redox peak analysis is the most simple and essential method. In general, Tafel slope($\left[\frac{\partial E}{\partial \log j}\right]_{pH}$), pH dependence of voltage at specific current density($\left[\frac{\partial E}{\partial pH}\right]_j$) is required for electrokinetics study in OER field to derive reaction order on proton concentration($\left[\frac{\partial \log j}{\partial pH}\right]_E$). Reaction order on proton concentration is interconnected with Tafel slope and pH dependence by below equation.

$$\left[\frac{\partial E}{\partial pH}\right]_j = -\left[\frac{\partial E}{\partial \log j}\right]_{pH}\left[\frac{\partial \log j}{\partial pH}\right]_E \qquad (4)$$

Thus, if two values out of them are known, we can calculate the value of remaining one. Tafel slope means required voltage to increase one order of current density. Low Tafel slope means that some catalyst are more efficient in the high potential region. In addition to this, Tafel slope can provide information on the number of electrons which are involved in the reaction before rate determining step of oxygen evolution reaction. This information is very useful when scientists hypothesize mechanism of electrochemical

reaction. Reaction order means dependence of reaction rate on the concentration of reactant. Usually in OER field, reaction order indicates log current density dependence on pH. This value provide information about the number of proton involved in the reaction before rate determining step of oxygen evolution reaction. Therefore, if information about Tafel slope and reaction order on proton concentration is obtained, people can understand that how many electrons and protons participate in the reaction before rate determining step, which is a part of reaction mechanism. Thus, we first measured catalytic property of Mn_3O_4, Mn_2O_3, Mn_5O_8 in pH 7, pH 7.5 and pH 8.0 to observe pH dependence of potential at specific current density. We decided 1 mA/cm^2 as standard specific current density to exclude effect of charging current. pH dependence results of various manganese oxide nanoparticles are shown in figure 3.9, 3.10 and 3.11. Next, we conducted Tafel slope analysis. Tafel slope is expressed as below equation. b(Tafel slope) = 2.3RT/nF. n is the number of electrons involved in the reaction before rate determining step. As shown in figure 3.12, Tafel slope of Mn_3O_4, Mn_2O_3 and Mn_5O_8 was 53.8 mV/dec, 57.7 mV/dec and 50.9 mV/dec, respectively. Typically, 50~80 mV/dec of Tafel slope indicates that one electron transfer is involved prior to rate determining step during oxygen evolution reacation. Using Tafel slope and pH dependence results, we calculated reaction order on proton concentration. Its values were 0.9(1), 0.91(1) and 2.2(2) for Mn_3O_4, Mn_2O_3 and Mn_5O_8, respectively. Therefore, we concluded that one electron and one proton transfer is involved prior to rate determining step for Mn_3O_4 and Mn_2O_3 while one electron and two proton transfer is involved prior to rate determining step for Mn_5O_8. In other words, this result means that mechanism

of Mn_3O_4 and Mn_2O_3 is different from that of Mn_5O_8. There is a possibility that different OER mechanism resulted in different OER activity between Mn_3O_4, Mn_2O_3 and Mn_5O_8 nanoparticles which is shown in figure 3.7. These electrokinetics results are summarized into the Table 3.1. Further, we compared redox peak of manganese oxide nanoparticles to obtain another information about the OER mechanism. As we can see in figure 3.13, Mn_3O_4 and Mn_5O_8 nanoparticles which have divalent manganese species in their crystal structure, showed redox peak before oxygen evolution reaction starts. However, sintered Mn_2O_3 nanoparticles which have only trivalent manganese species in the crystal structure showed no redox peak before catalysis begins. Also, Mn_2O_3 showed a little bit earlier reaction onset than Mn_3O_4 and Mn_5O_8 nanoparticles. There are previous reports that manganese oxide starts oxygen evolution reaction after divalent manganese species is oxidized into trivalent manganese ion because trivalent manganese species is important intermediate for oxygen evolution reaction. The result of previous research is matched with our redox peak analysis result.

Based on the electrokinetics and redox peak analysis, we suggested oxygen evolution reaction mechanism of manganese oxide nanoparticles assuming that oxygen-oxygen bond formation is rate determining step of OER.

Figure 3.14 shows OER mechanism of Mn_3O_4 and Mn_2O_3 nanoparticles. First, initial state is oxidized to catalytic resting state including Mn^{3+} by redox reaction which is observed in figure 3.13. Sintered Mn_2O_3 nanoparticles, which consist of trivalent manganese species already, exist as catalytic resting state at first. We think Mn_2O_3 begins OER earlier than other materials due to this reason. Then, one electron and proton is transferred from Mn(III)-OH

species of resting state, resulting in Mn(III)-oxygen radical species. Involvement of one electron and one proton is calculated by electrokinetics study. In the next step, oxygen-oxygen bond is formed, which is rate determining step. Oxygen is generated after this step.

Somewhat different OER mechanism of Mn_5O_8 is shown in Figure 3.15. First, initial state is oxidized to catalytic resting state including Mn3+ by redox reaction which is observed in figure 3.13. Then, additional intermediate state is added in the OER of Mn_5O_8 unlike Mn_3O_4 and Mn_2O_3. Because of low PK_a value of Mn(IV), proton is reduced from Mn(IV)-OH species. Then, one electron and proton is transferred from Mn(III)-OH species of this intermediate state, resulting in Mn(III)-oxygen radical species. Involvement of one electron and two proton is calculated by electrokinetics study. In the next step, oxygen-oxygen bond is formed, which is rate determining step. Oxygen is generated after this step.

Detailed process after rate determining step is omitted here because experimental evidence is not enough to suggest mechanism. Therefore, further study is required for complete understanding on mechanism of manganese oxide nanoparticles. Although we couldn't identify all the process of OER mechanism of manganese oxide nanoparticles, we think that different OER mechanism of Mn_5O_8 caused less active OER property of Mn_5O_8 nanoparticles than other manganese oxide nanoparticles because one more intermediate state is needed.

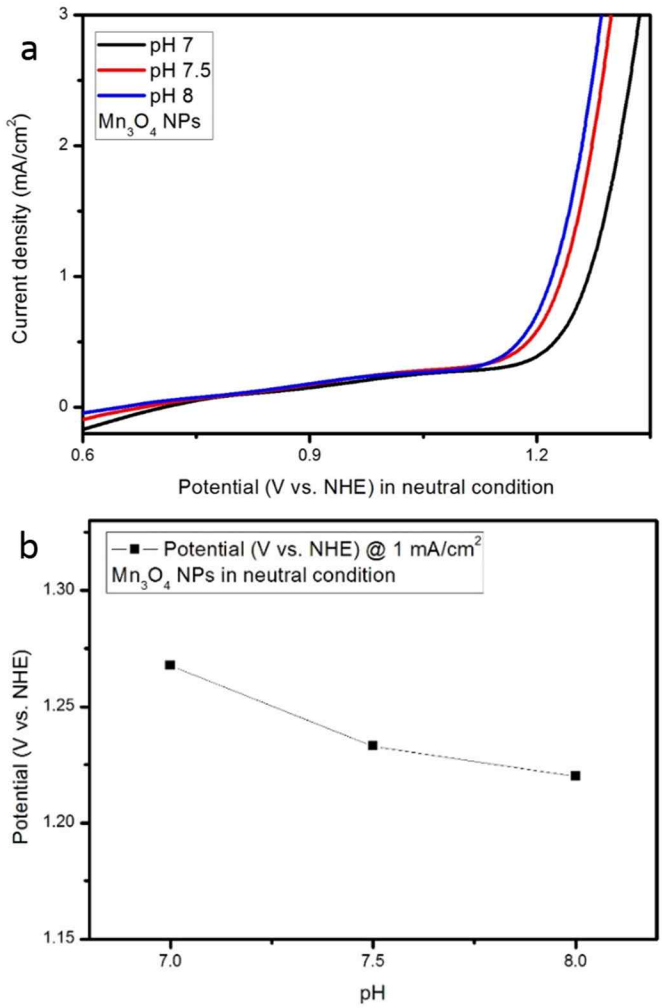

Figure 3.9 pH dependence experiment of Mn_3O_4 nanoparticles. (a) Polarization curves of Mn_3O_4 nanoparticles at pH 7, pH 7.5 and pH 8 in a 0.3 M phosphate buffer solution. Scan rate: 0.01 V/s. (b) pH dependence data obtained from (a).

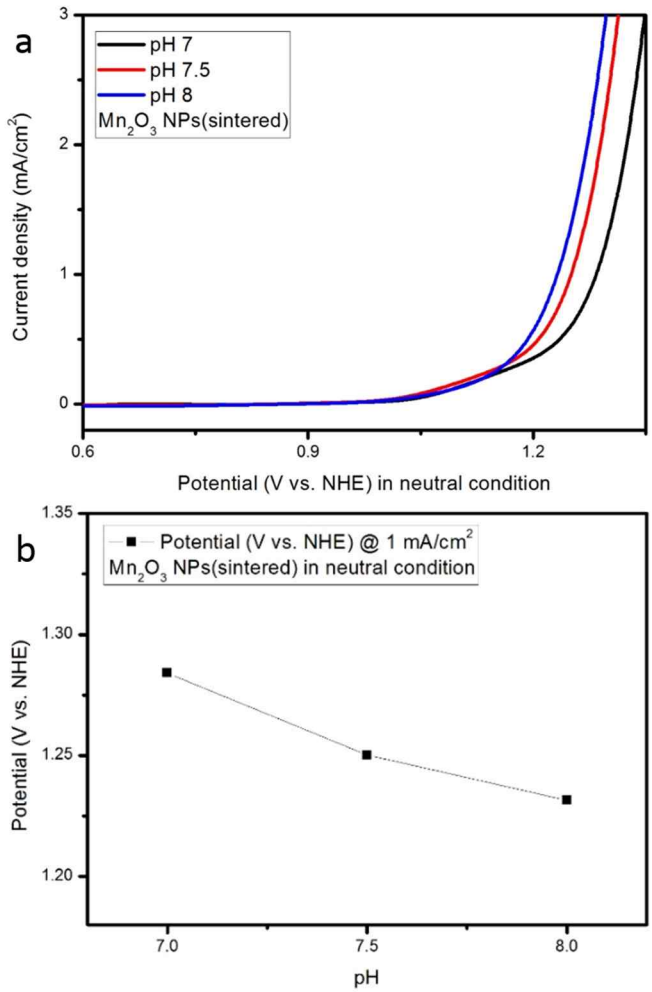

Figure 3.10 pH dependence experiment of Mn_2O_3 sintered nanoparticles. (a) Polarization curves of Mn_2O_3 sintered nanoparticles at pH 7, pH 7.5 and pH 8 in a 0.3 M phosphate buffer solution. Scan rate: 0.01 V/s. (b) pH dependence data obtained from (a).

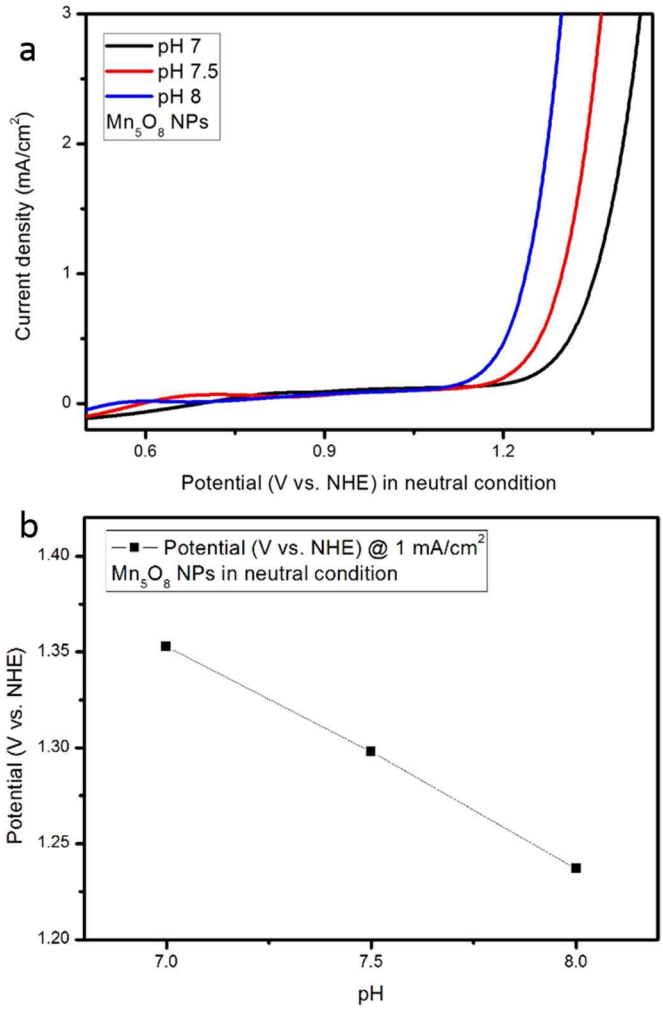

Figure 3.11 pH dependence experiment of Mn_5O_8 nanoparticles. (a) Polarization curves of Mn_5O_8 nanoparticles at pH 7, pH 7.5 and pH 8 in a 0.3 M phosphate buffer solution. Scan rate: 0.01 V/s. (b) pH dependence data obtained from (a).

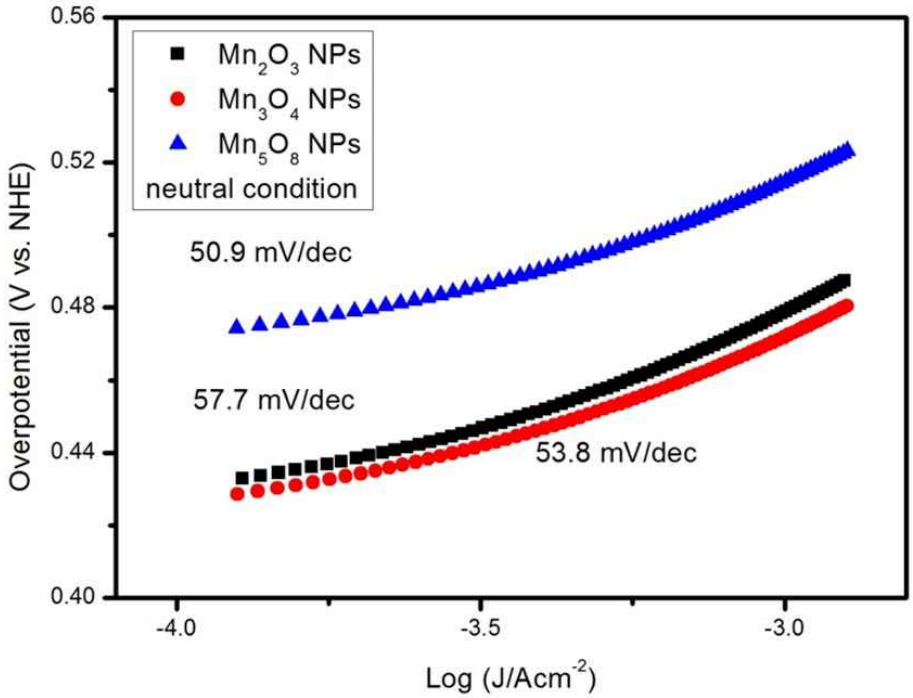

Figure 3.12 Tafel slope analysis of manganese oxide nanoparticles

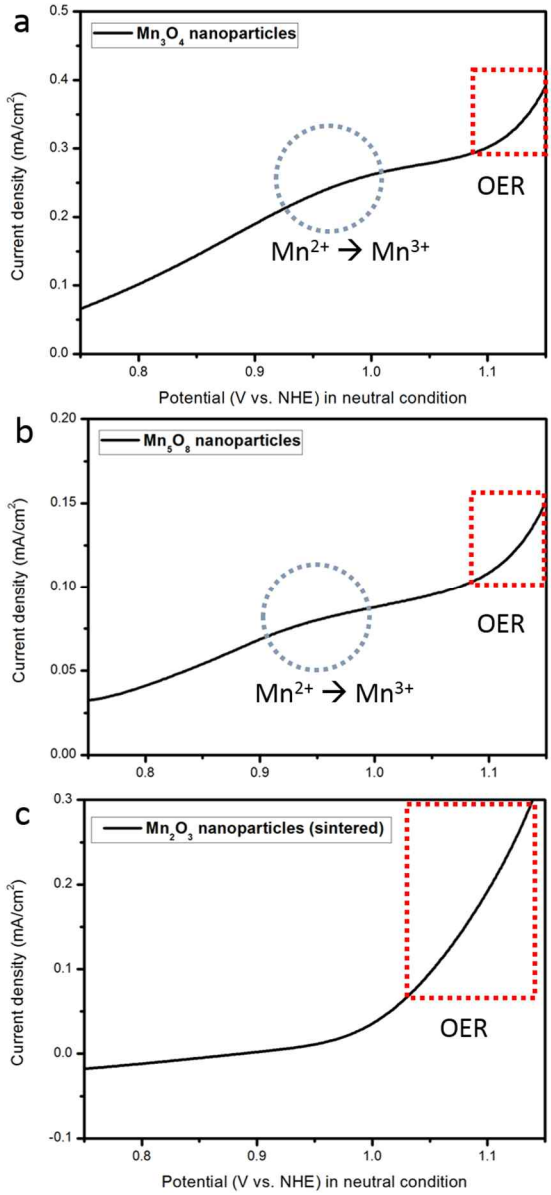

Figure 3.13 Redox peak analysis of manganese oxide nanoparticles. (a) Mn_3O_4 nanoparticles, (b) Mn_5O_8 nanoparticles, (c) Mn_2O_3 sintered nanoparticles.

Table 3.1 Summary of electrokinetics study on manganese oxide nanoparticles

Catalyst	pH dep (mV/pH)	Tafel slope (mV/dec)	Involved proton	Before RDS
Mn_2O_3	-52.6	57.7	0.91(1)	1 e^-, 1 H^+
Mn_3O_4	-48.4	53.8	0.90(1)	1 e^-, 1 H^+
Mn_5O_8	-112.1	50.9	2.20(2)	1 e^-, 2 H^+

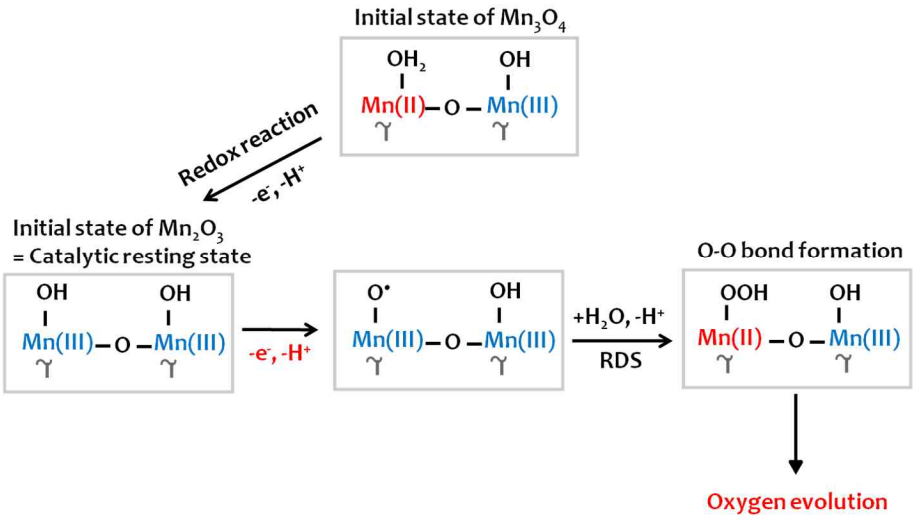

Figure 3.14 Proposed OER mechanism of Mn_3O_4 and Mn_2O_3 nanoparticles.

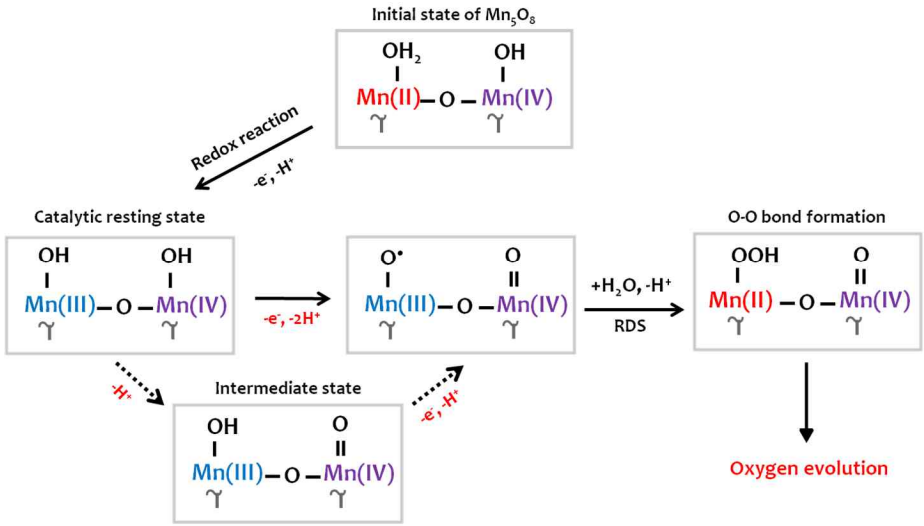

Figure 3.15 Proposed OER mechanism of Mn_5O_8 nanoparticles

3.3 Effect of nano size on the catalytic property

In previous chapter, various manganese oxide nanoparticles was synthesized and their catalytic property was compared to confirm that various claims on catalytic activity enhancement factor of bulk materials are applicable in nano sized materials. Using this material, we compared the OER property of manganese oxide nanoparticles with bulk materials with same phase to identify nano size effect. As shown in figure 3.16, nanoparticles showed much higher OER activity than bulk materials with same phase. From this result, we thought that the substantial activity difference is originated from various factor, including surface area effect. Therefore, we conducted further research to identify the factor contributing to high activity of nanoparticles. Among the various manganese oxide materials, we chose Mn_5O_8 as model material because it has never been investigated as OER catalysts.

3.3.1 Characterization of Mn_5O_8 materials

For the synthesis of the Mn_5O_8 NPs, 13 nm sized spherical MnO NPs were first synthesized by a modified heat up method. (See experimental procedures for details.) The morphology of the MnO NPs were characterized using scanning electron microscopy (SEM) and transmission electron microscopy (TEM) analysis (Figure 3.17 and figure 3.19).

Then, MnO NPs were converted to Mn_5O_8 NPs via annealing under the same condition which is mentioned before. From the PXRD, SEM and TEM analysis, it was shown that the obtained NPs were Mn_5O_8 (Figure 3.20d), and

there was no observable change in morphology or size after the heat treatment (Figure 3.20a and 3.20b).

Next, micron sized Mn_5O_8 particles were synthesized to compare the catalytic activity and stability with Mn_5O_8 nanoparticles. The γ-MnOOH precursor was prepared using the conventional hydrothermal method, and it was changed via a two-step heat treatment(γ-MnOOH --> Mn_3O_4 --> Mn_5O_8). Annealing condition to obtain micron sized Mn_5O_8 was different from the condition which was used for Mn_5O_8 nanoparticles. The phase of the precursor materials(γ-MnOOH and Mn_3O_4) was confirmed by powder X-ray diffraction analysis whose result is shown in figure 3.19. From this result, we could observe that micron sized Mn_3O_4 and Mn_5O_8 particles have poor quality of XRD than γ-MnOOH. This phenomenon is due to size reduction and phase transformation without sintering. Phase transformation without sintering can cause crystallinity decrease because of insufficient time for diffuse of atom. Also, it is widely known that small size particle has broader XRD peak than large size particle. The morphology of the precursor materials was confirmed by scanning electron microscopy image which is shown in figure 3.18. The obtained Mn_5O_8 compounds were rod-shaped with a micron sized length and a 100 nm diameter. From this image, we can clearly see that Mn_3O_4 and Mn_5O_8 has smaller particle size than γ-MnOOH, which is matched result with the aforementioned reason. This phenomenon is observed again when Mn_5O_8 nanoparticles are compared with micron sized Mn_5O_8 in figure 3.20d. In figure 3.20, the morphology and crystallinity difference between Mn_5O_8 materials is clearly shown.

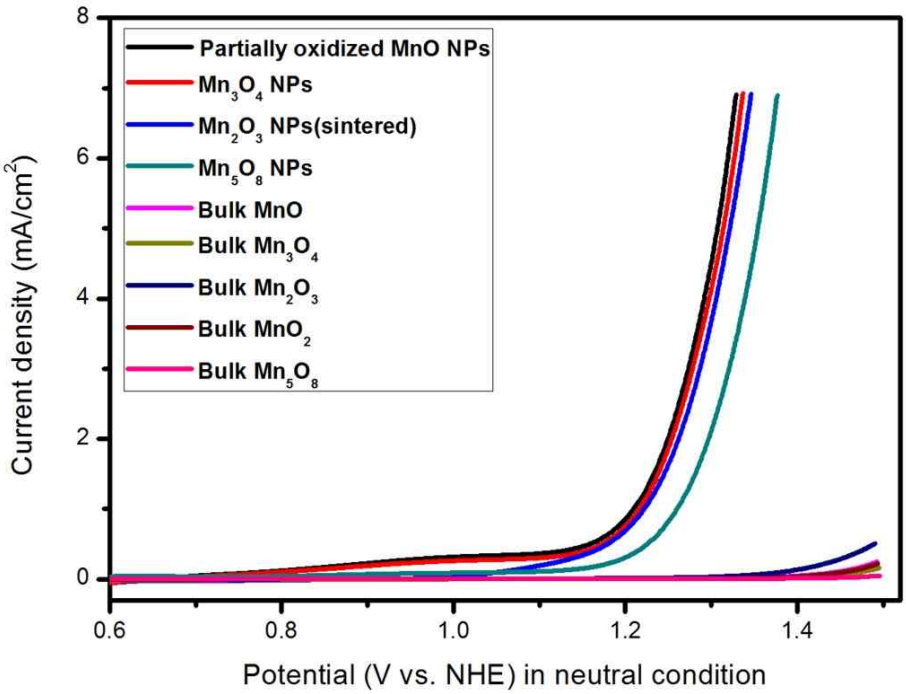

Figure 3.16 Polarization curves of manganese oxide nanoparticles including bulk materials at pH 7.8 in a 0.3 M phosphate buffer solution. Scan rate: 0.01 V/s

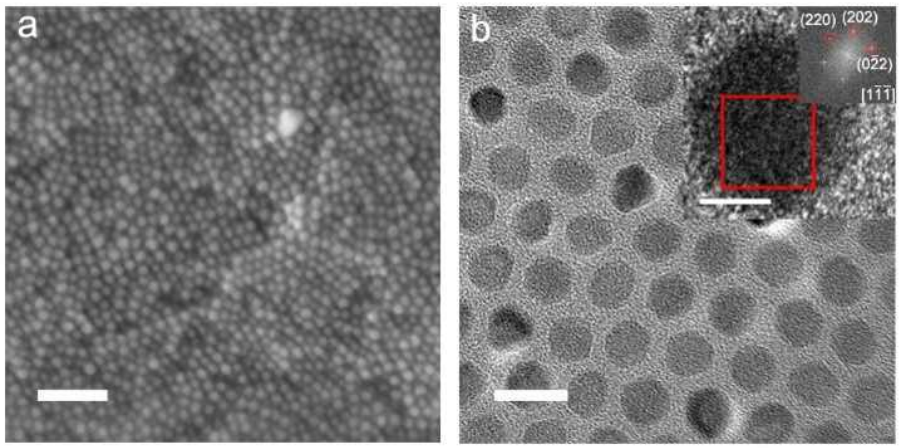

Figure 3.17 (a) SEM image of MnO nanoparticles. (Scale bar: 100 nm)
(b) TEM image of MnO nanoparticles. (Scale bar: 20 nm. Inset scale bar: 5 nm)

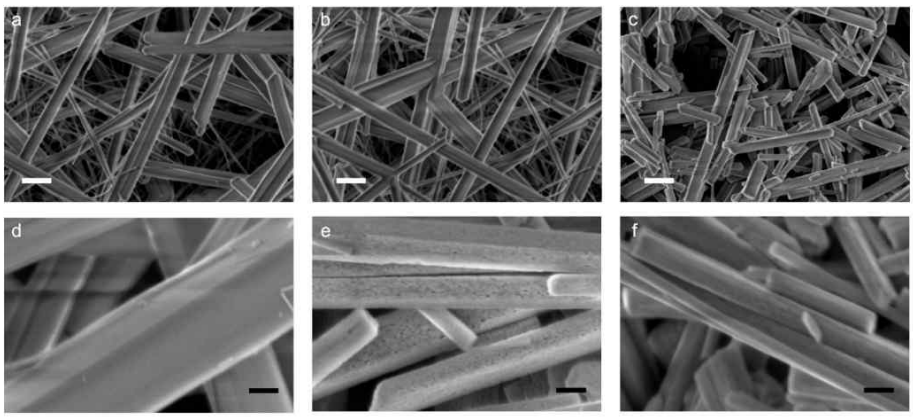

Figure 3.18 SEM image of (a,d) micron-sized γ-MnOOH, (b,e) micron-sized Mn_3O_4 and (c,f) micron-sized Mn_5O_8. Scale bar in (a,b,c): 400 nm; scale bar in (d,e,f): 100 nm

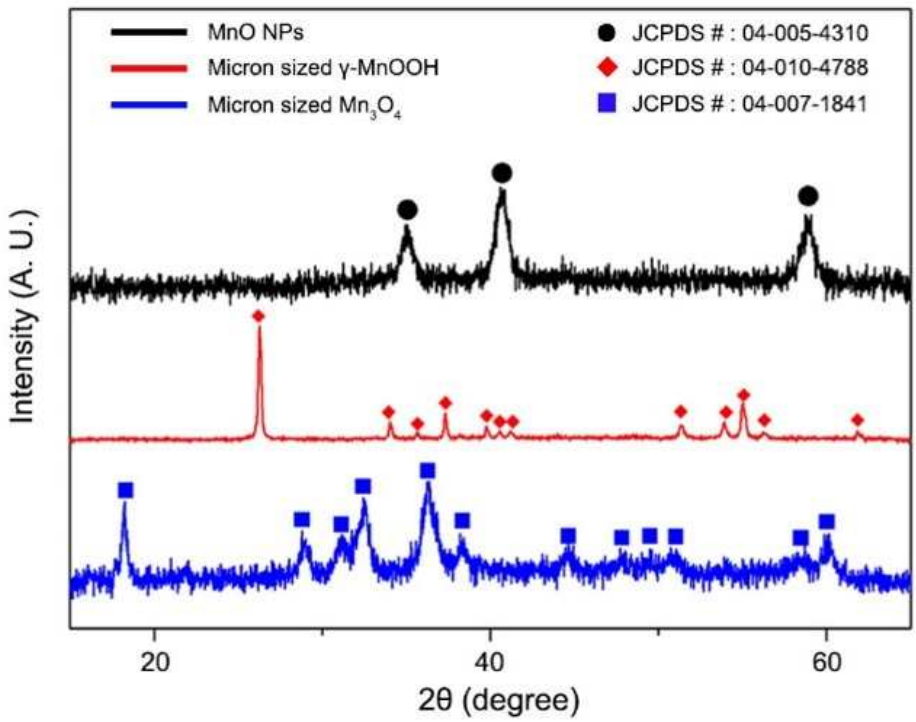

Figure 3.19 Powder X-ray diffraction results of Mn_5O_8 precursor materials. Black line: As-prepared MnO nanoparticles; Red line: micron sized γ-MnOOH; Blue line: micron sized Mn_3O_4 particles

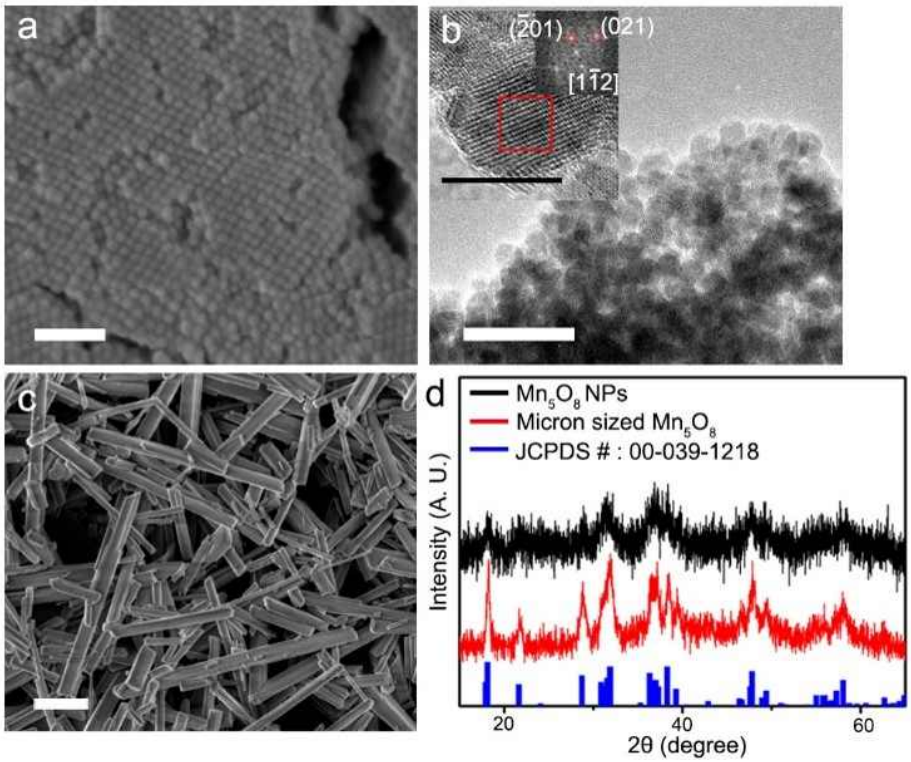

Figure 3.20 Characterization of Mn_5O_8. (a) SEM image of Mn_5O_8 NPs (scale bar: 100 nm). (b) TEM image of Mn_5O_8 NPs (scale bar: 50 nm, inset scale bar: 10 nm). (c) SEM image of micron sized Mn_5O_8 (scale bar: 600 nm). (d) PXRD data of Mn_5O_8 materials.

3.3.2 Catalytic activity comparison of Mn_5O_8 materials

The activity of the Mn_5O_8 NPs for OER catalysis was evaluated using cyclic voltammetry (CV). The Mn_5O_8 NPs were prepared on a fluorine-doped tin oxide (FTO) glass substrate using spin coating. (See the experimetnal procedures for the cell preparation details.) The evaluation for OER activity was performed at pH 7.8 and in a 0.3 M sodium phosphate buffer solution. The high activity of the Mn_5O_8 NPs under near neutral conditions is displayed in Figure 3.22. Because there are no previous reports on the OER properties of Mn_5O_8 NPs, we first should confirm that the recorded current density was originated from the oxygen evolution reaction. Therefore, faradaic efficiency measurement was conducted. Faradaic efficiency means the efficiency with which electrons are transferred in electrochemical system. Calculated faradaic efficiency was 92 % for Mn_5O_8 nanoparticles,, indicating that the measured current was originated from oxygen evolution (figure 3.21). After then, we synthesized well-known OER electrocatalysts, such as CoPi and MnOx, using the electrodeposition method, to estimate the catalytic property of Mn_5O_8 nanoparticles. As shown in figure 3.22, the OER properties of the Mn_5O_8 NPs were similar to those of CoPi and were markedly better than those of electrodeposited MnO_x. For the precise comparison, the OER properties of various electrocatalysts are summarized in table 3.2 including noble metal oxide. From this result, it was identified that Mn_5O_8 nanoparticles efficiently oxidize water in neutral condition. The activity of micron sized Mn_5O_8 particles for OER catalysis was also evaluated using cyclic voltammetry (CV).

As shown in figure 3.23, micron sized Mn_5O_8 particles showed poor catalytic activity because large particle size reduces interface area between micron sized Mn_5O_8 particles, decreasing electron conductivity. For enhancement of electron conductivity, vulcan carbon was added into ink of micron sized Mn_5O_8 particles. As a result, catalytic property was drastically enhanced.(Figure 3.23) Thus, we compared mass activity and the Tafel slope of Mn_5O_8 nanoparticles and micron sized particles(with carbon) to investigate the effect of particle size on the catalytic properties. As shown in figure 3.24, Mn_5O_8 nanoparticles showed much higher catalytic activity than micron sized Mn_5O_8 when sample was made with the same amount of catalyst loading. At the overpotential of 610 mV, the mass activity of the Mn_5O_8 NPs was 116 A/g whose value is about 20 times higher than that of micron-sized Mn_5O_8(5.7 A/g). To understand the origin of this activity difference, Brunauer-Emmett-Teller (BET) analysis was performed. The surface area of the Mn_5O_8 NPs and the rods was determined as 41.83 and 12.93 m^2/g, respectively. Although the Mn_5O_8 NPs have higher surface area than the micron sized Mn_5O_8 particles, the difference cannot fully explain the substantial activity difference between them. In addition, the Mn_5O_8 NPs had a lower Tafel slope (78.7 mV/dec) than the micron sized Mn_5O_8 (154 mV/dec), indicating that the Mn_5O_8 NPs are more efficient than the micron-sized Mn_5O_8 in the high potential region.

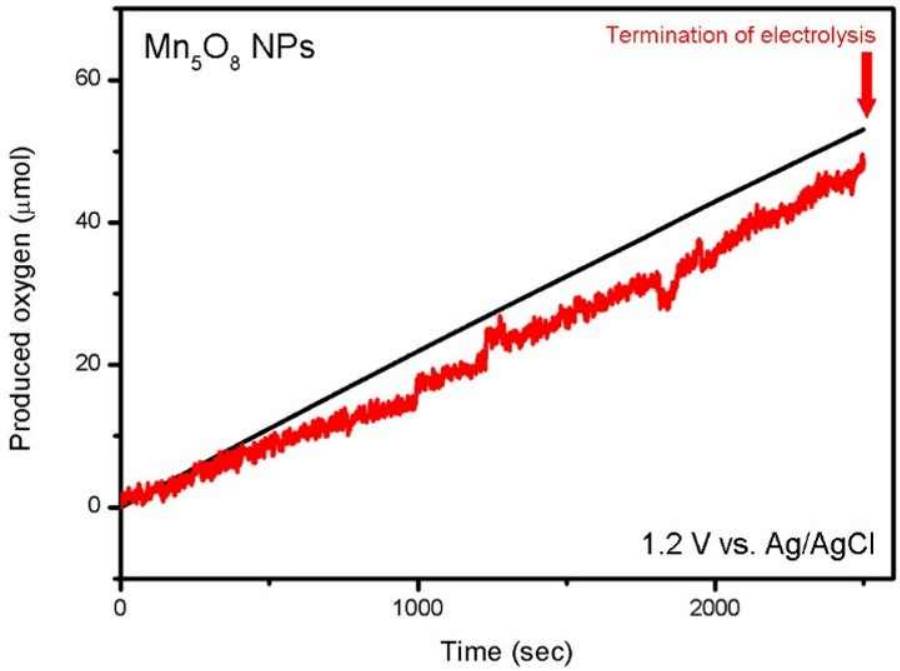

Figure 3.21 The amount of produced oxygen molecules measured by experimental amount (red line) and the theoretical amount (black line) of evolved oxygen during bulk electrolysis. The theoretical amount of oxygen molecules was plotted assuming a faradaic efficiency of 100 %. Calculated faradaic efficiency is 92 %.

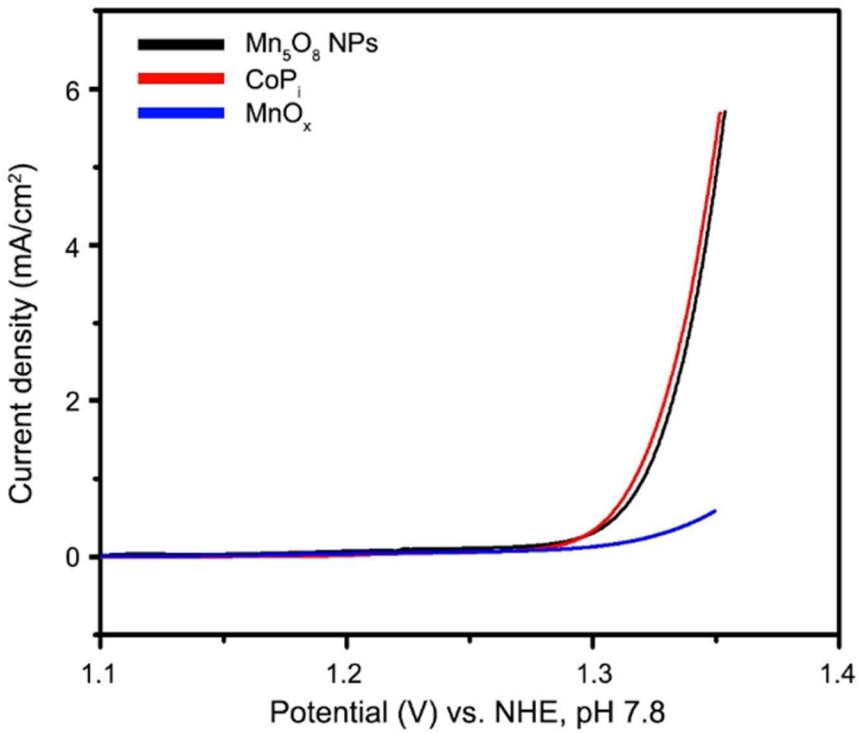

Figure 3.22 Polarization curves of Mn_5O_8 nanoparticles, CoP_i and MnO_x at pH 7.8 in a 0.3 M phosphate buffer solution. Scan rate: 0.01 V/s

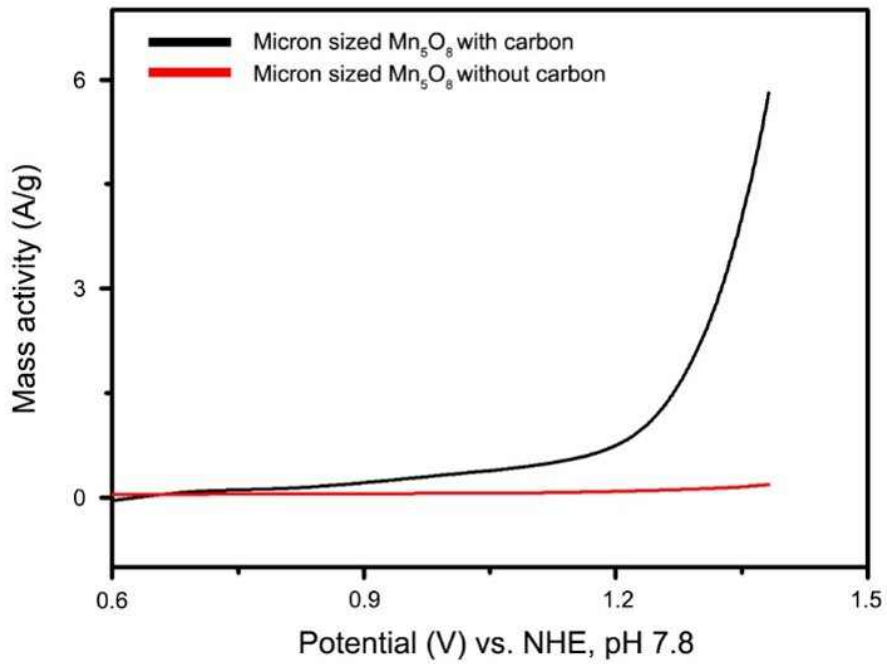

Figure 3.23 Effect of Vulcan carbon on mass activity of micron sized Mn_5O_8. Cyclic voltammetry curve is polarized.

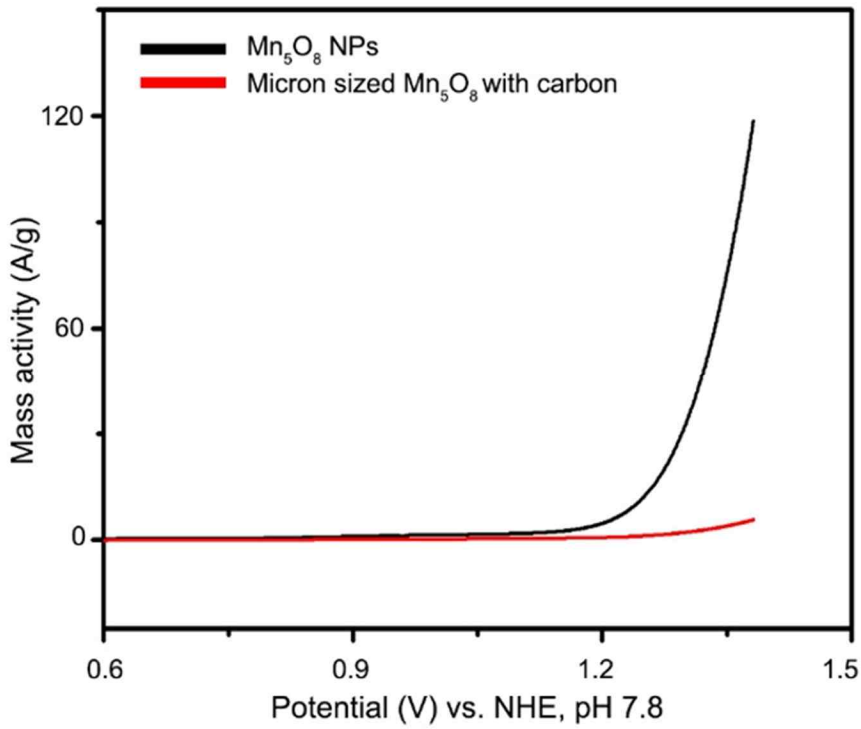

Figure 3.24 Mass activity comparison data between Mn_5O_8 nanoparticles and micron sized Mn_5O_8 with carbon (inset image: Tafel slope of Mn_5O_8 materials). Scan rate: 0.01 V/s

Table 3.2 Information about various electrocatalysts

Catalyst	Preparation method	Overpotential @ pH 7.8	BET (m^2/g)	Notes
Mn_5O_8 NPs	Spin coating	580 mV (@ 5 $mAcm^{-2}$)	41.83	This work
Mn_5O_8 rod	Drop casting	700 mV (@ 1 $mAcm^{-2}$)	12.93	This work Vulcan C added
Co-Pi	Electrodeposition	570 mV (@ 5 $mAcm^{-2}$)	N. A.	Reproduced with the previous method[3]
MnO_x	Electrodeposition	600 mV (@ 1 $mAcm^{-2}$)	N. A.	Reproduced with the previous method[4]
IrO_x	Electrodeposition	310 mV (@ 5 $mAcm^{-2}$)	N. A.	Extrapolation from the previous method [5]

3.3.3 Catalytic stability comparison of Mn_5O_8 materials

To compare the catalytic stability of the Mn_5O_8 nanoparticles and micron sized particles, bulk electrolysis (BE) experiment was conducted. Bulk electrolysis of Mn_5O_8 materials was recorded at 1.2 V vs. Ag/AgCl for 5000 seconds. As shown in figure 3.25, Mn_5O_8 nanoparticles (black line) showed moderate electrochemical stability while micron sized Mn_5O_8 became inactive in an instant during OER. This result indicates that Mn_5O_8 nanoparticles are intrinsically stable OER catalyst unlike micron sized Mn_5O_8 particles. After then, we tried to enhance electrochemical stability of Mn_5O_8 nanoparticles using Nafion solution. First, we adjusted pH of Nafion solution(acid) to 7 because manganese oxide is dissolved in acidic solution. After then, neutralized Nafion solution was dropped onto the Mn_5O_8 nanoparticles film. As a result, Mn_5O_8 NPs showed improved stability at 1.3 V vs. Ag/AgCl (red line in figure 3.26b) because neutralized Nafion solution prevented particle detachment from FTO substrate. In the meantime, We noted that the electrolysis curves of the Mn_5O_8 NPs with Nafion are slightly bumpy. That is because oxygen bubbles produced during the OER is captured and emitted inside the films. Further, we conducted long cycle CV for Mn_5O_8 nanoparticles, which shows stable redox activity of Mn_5O_8 nanaparticles (figure 3.27). These results show that Mn_5O_8 nanoparticles itself is catalytically stable only if physical detachment is prevented.

After then we conducted SEM and TEM analysis of Mn_5O_8 nanoparticles after bulk electrolysis to confirm that Mn_5O_8 nanoparticles are stable in structural view. From SEM image in figure 3.28, it was shown that morphology of

Mn_5O_8 nanoparticles doesn't change during OER. In addition to that, figure 3.29 shows that amorphization did not occur on the surface of Mn_5O_8 nanoparticles. FFT analysis of TEM image was also conducted to support the phase stability of Mn_5O_8 nanoparticles. As a result, it was confirmed that the Mn_5O_8 phase was maintained after oxygen evolution reaction, indicating high phase stability (Figure 3.29, inset).

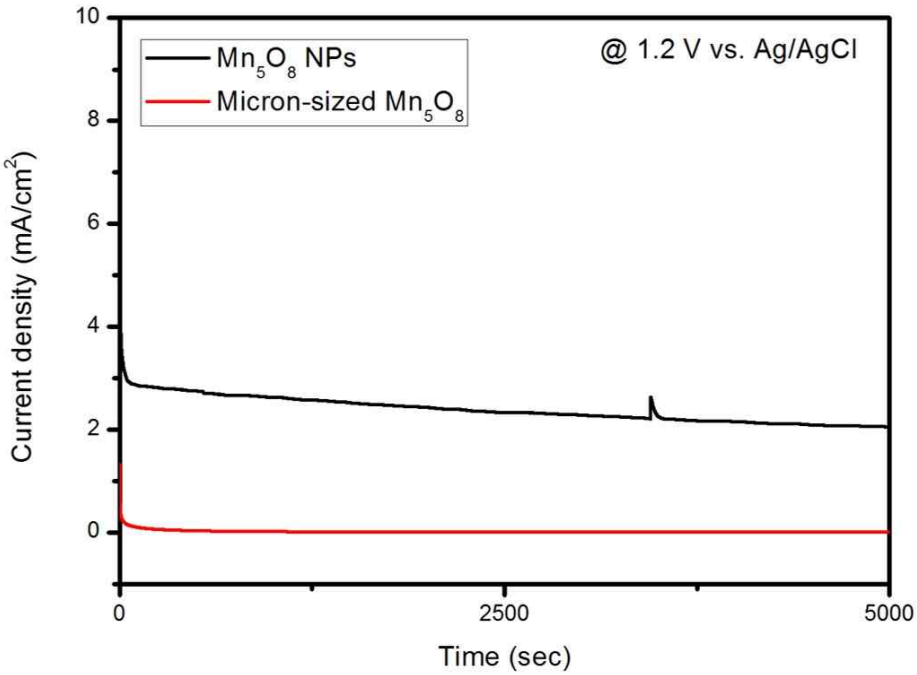

Figure 3.25 Bulk electrolysis curve of Mn_5O_8 materials at pH 7.8 in a 0.3 M phosphate buffer solution

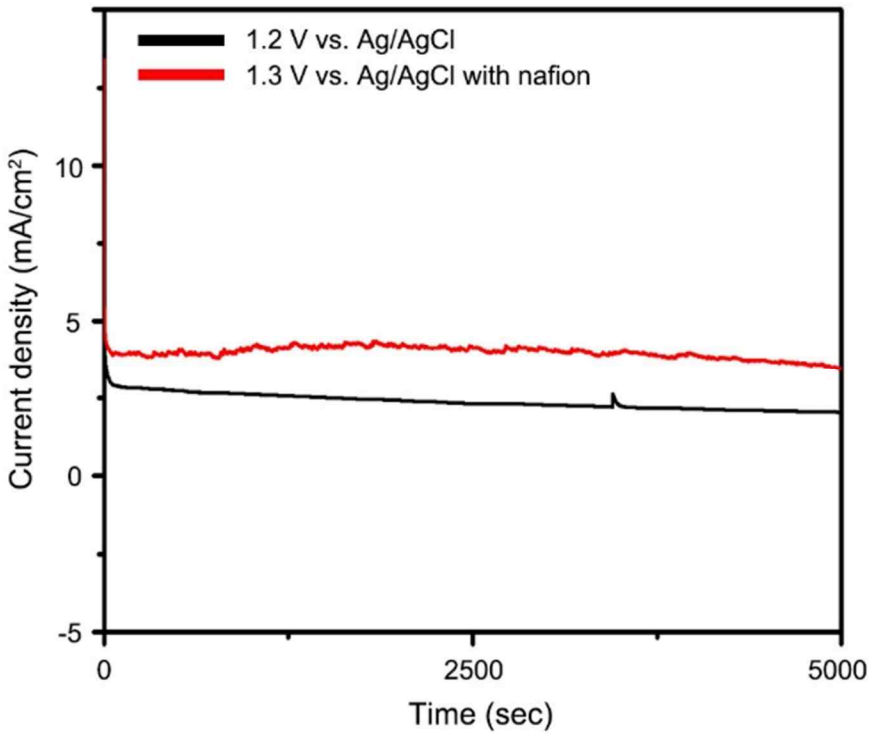

Figure 3.26 Effect of Nafion film on catalytic stability of Mn_5O_8 nanoparticles.

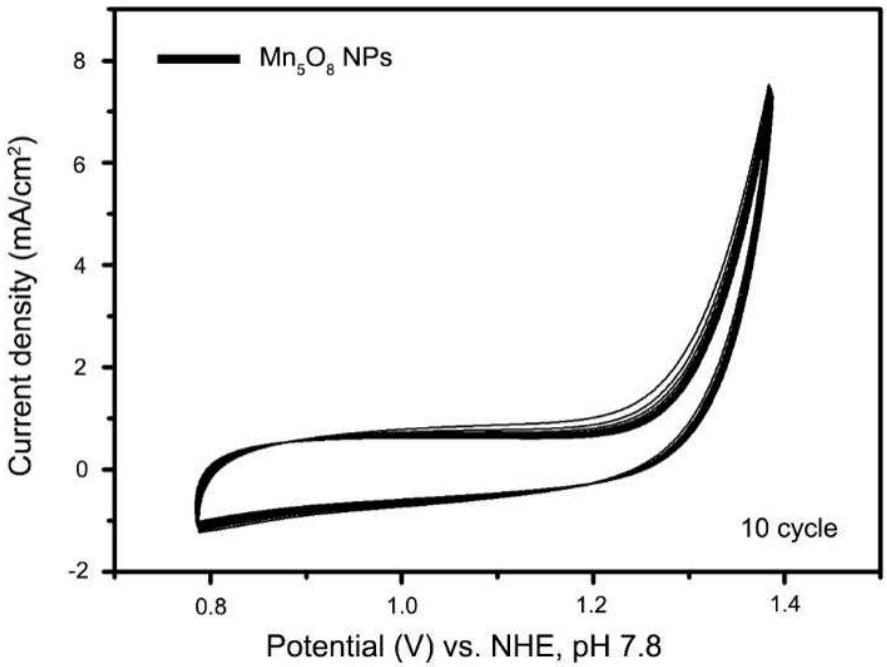

Figure 3.27 Long cyclic voltammetry curve of Mn_5O_8 NPs under near neutral condition. Scan rate: 0.1 V/s

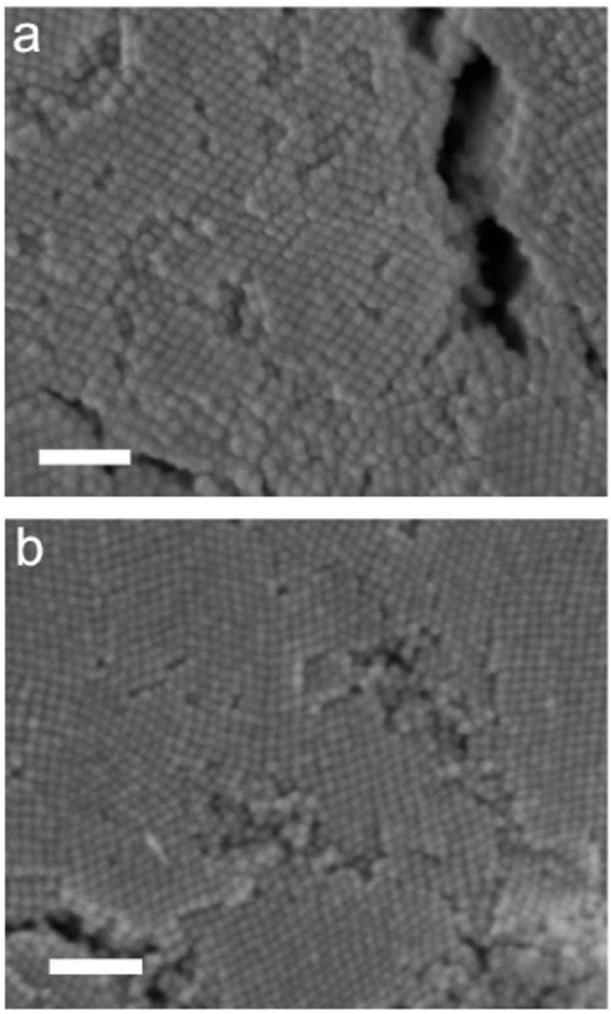

Figure 3.28 SEM image of Mn_5O_8 NPs (a) before and (b) after bulk electrolysis at 1.2 V (vs. Ag/AgCl) for 3600 seconds. Scale bar: 100 nm

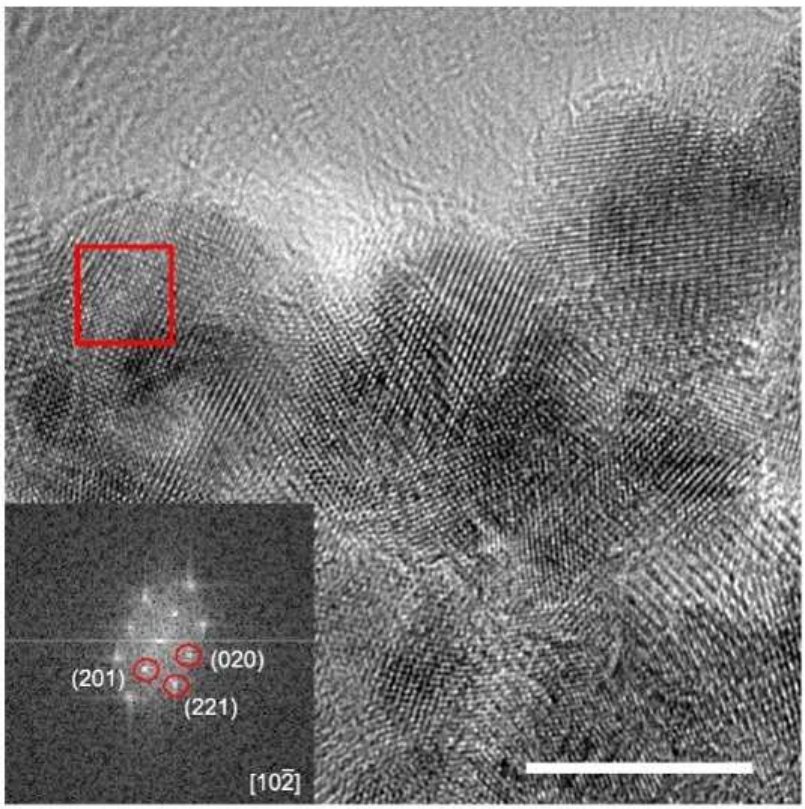

Figure 3.29 TEM image of Mn_5O_8 NPs after bulk electrolysis at 1.2 V (vs. Ag/AgCl) for 3600 seconds. Inset: FFT analysis result. Scale bar: 10 nm

3.4 Electron Paramagnetic Resonance (EPR) analysis

Considering the results of catalytic property comparison, we thought that an intrinsic difference exists between the Mn_5O_8 NPs and the micron sized Mn_5O_8 particles. To reveal the origin of this intrinsic difference, we focused on the manganese valence behavior of Mn_5O_8 materials during catalysis because we confirmed the validity of hypothesis that Mn^{3+} affects the oxygen evolution property of manganese oxide nanoparticles.

In this study, Electron Paramagnetic Resonance (EPR) techniques were adopted to monitor the manganese valence behavior of Mn_5O_8 materials during the catalysis. Catalyst ink with the same amount of Mn_5O_8 NPs and micron sized Mn_5O_8 particles was loaded onto the FTO electrode to precisely compare their activity. We applied 1.25 V (vs. Ag/AgCl) to the catalyst film for 1,000 seconds to observe valence behavior of manganese during the catalysis. Additionally, pyrophosphate (PP) solution was employed to prepare the EPR sample because pyrophosphate is known as a redox-inactive material that can capture Mn^{3+} species. To prevent further electron transfer in the materials after catalytic reaction, we froze each EPR sample with liquid nitrogen immediately after mixing the catalyst with other substances. (See the experimental procedures for preparation details.)

The X-band EPR spectra are recorded to show the behavior of Mn^{2+} and Mn^{3+} of Mn_5O_8 materials. As revealed in figure 3.30, typical Mn^{2+} EPR signal with the six-line splitting around 3413 G (g~2) was detected in both as-prepared Mn_5O_8 samples(nanoparticles and micron sized particles). Also, carbon radical signal appeared around 3440 G (g~2) in the perpendicular

mode EPR spectra because we mixed Vulcan carbon with catalysts to enhance electron transfer. (perpendicular mode means microwave(H_1 field) and magnetic field(H_0 field) is perpendicular.) In addition to this, low intensity of Mn^{3+} EPR signal with the six-line hyperfine splitting centered at 820 G (g_{eff} ~ 8.2) was observed in only as-prepared Mn_5O_8 nanoparticles when using parallel mode EPR spectra.(parallel mode means micro-wave(H_1 field) and magnetic field(H_0 field) is parallel.) This means that a little bit of Mn^{3+} species exists in Mn_5O_8 nanoparticles unlike micron sized Mn_5O_8 particles in as-prepared state.

This difference was maximized right after oxygen evolution reaction. Comparing figure 3.30a with Figure 3.31a, Mn^{2+} of Mn_5O_8 disappears right after the OER, which means that Mn^{2+} is oxidized to higher valence during catalysis. The Mn^{3+} signal was enhanced immediately after the OER for both of the Mn_5O_8 materials (Figure 3.30b and Figure 3.31b). To confirm that enhanced Mn^{3+} signal after OER is not affected by PP, EPR measurement was conducted again with as-prepared Mn_5O_8 nanoparticles after waiting 10 minutes in ambient atmosphere. As shown in figure 3.32, there was no significant change of Mn^{3+} signal for Mn_5O_8 nanoparticles, indicating that enhanced Mn^{3+} signal after OER was due to the catalytic reaction.

Therefore, above results indicate that Mn^{3+} is involved in the OER process of Mn_5O_8. More importantly, there is a large difference in the Mn^{3+} EPR intensity between the Mn_5O_8 nanoparticles and the micron sized Mn_5O_8 particles right after OER as shown in figure 3.31b. For the Mn_5O_8 nanoparticles, strong and well-resolved six-line hyperfine splitting is shown; however, weak and poorly resolved one occurs for the micron sized Mn_5O_8

particles, indicating that the Mn_5O_8 nanoparticles have much more Mn^{3+} species during the OER. This result shows the possibility that Mn^{3+} is generated more easily and intrinsically stable in the Mn_5O_8 nanoparticles than micron sized Mn_5O_8 particles.

We think that the higher catalytic activity and stability of Mn_5O_8 nanoparticles may be due to the improved stability of Mn^{3+} along with the increased surface area. These conclusion imply that catalytic property of certain phase can intrinsically change depending on the particle size, especially when size of particle becomes nanoscale.

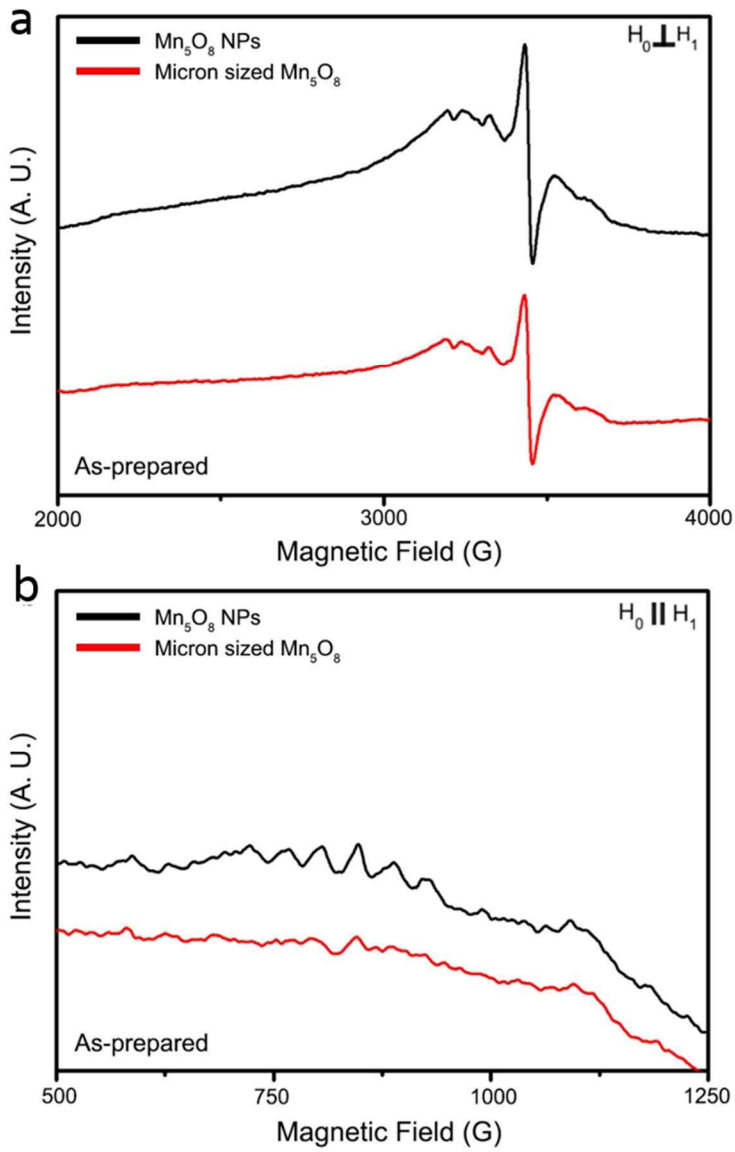

Figure 3.30 X-band EPR spectra of as prepared Mn_5O_8 materials.
(a) Perpendicular mode for Mn^{2+} detection, (b) Parallel mode for Mn^{3+} detection.
Y-axis scale of Figure 3.30a, 3.30b is same with that of Figure 3.31a and 3.31b.

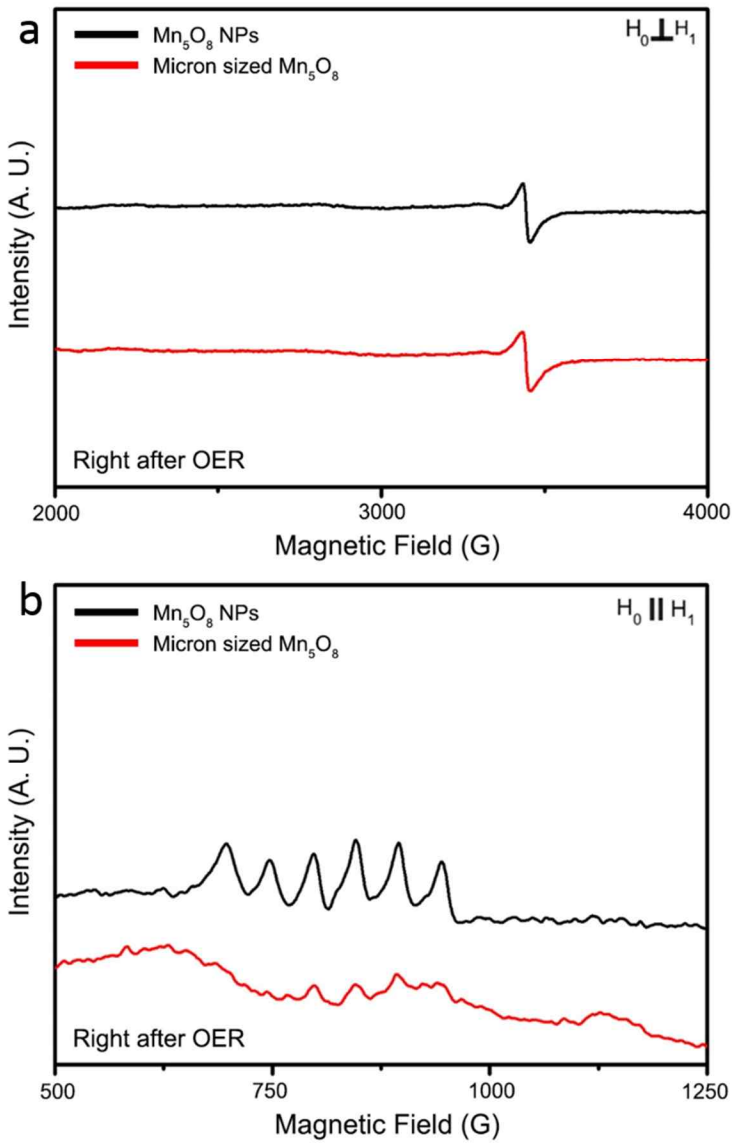

Figure 3.31 X-band EPR spectra of Mn_5O_8 materials right after OER.
(a) Perpendicular mode for Mn^{2+} detection, (b) Parallel mode for Mn^{3+} detection.
Y-axis scale of Figure 3.31a, 3.31b is same with that of Figure 3.30a and 3.30b

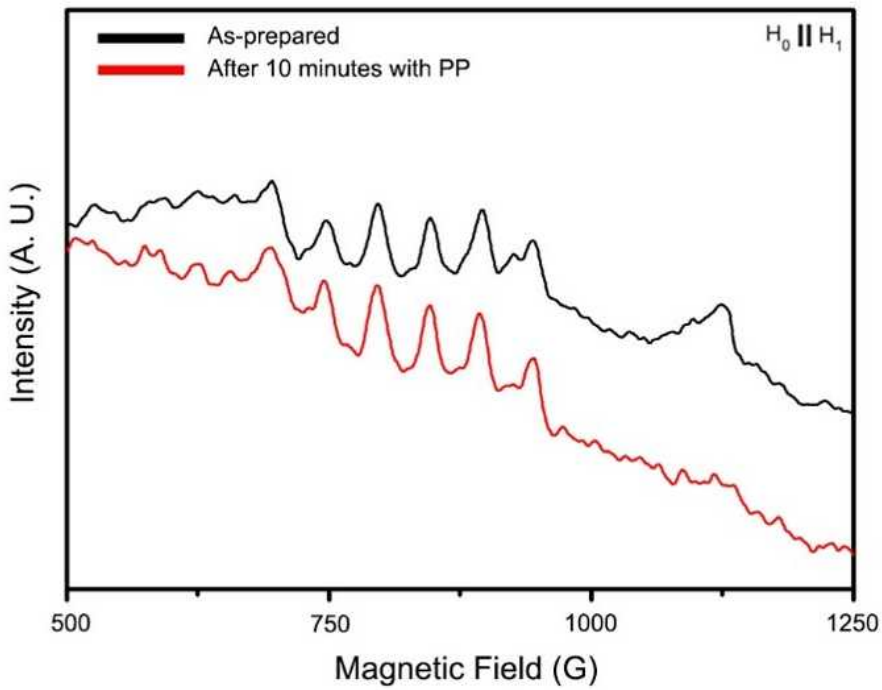

Figure 3.32 X-band parallel mode EPR spectra of as prepared Mn_5O_8 materials depending on the time with pyrophosphate solution

Chapter 4. Conclusion

In this research, we tried to investigate the effect of crystal structure on the OER activity of nano sized manganese oxide nanoparticles. First, we used 10 nm sized MnO nanoparticles as precursor material and transformed the phase into the various manganese oxide nanoparticles, Mn_3O_4, Mn_5O_8 and Mn_2O_3. Their catalytic activity was evaluated using cyclic voltammetry in near neutral condition. Mn_3O_4 and Mn_2O_3 showed similar activity and Mn_5O_8 showed less active property than Mn_3O_4 and Mn_2O_3. Based on this result, we confirmed that effect of crystal structure on catalytic activity is reduced in nano scale. To understand the reason of different activity between nanoparticles, we conducted electrokinetics and redox peak analysis. As a result, it was identified that OER mechanism of Mn_5O_8 was different from other materials in that Mn_5O_8 nanoparticles have one more intermediate state before RDS.

After then, we found that synthesized manganese oxide nanoparticles showed much higher catalytic property than bulk materials with same phase as we reported previously. Thus, we tried to understand what makes nanoparticles much more active catalyst than bulk manganese oxides with Mn_5O_8 as model system which has never been investigated in OER catalyst field. BET analysis and mass activity comparison clearly showed that Mn_5O_8 nanoparticles have much higher catalytic activity than micron sized Mn_5O_8 although surface area effect is excluded. In addition, catalytic stability is also enhanced in nanoparticles. These results imply that intrinsic catalytic property can change as particle size becomes nano scale. To reveal the origin of this intrinsic difference, we focused on the manganese valence behavior of Mn_5O_8

materials during catalysis because we confirmed the validity of hypothesis that Mn^{3+} affects the oxygen evolution property of manganese oxide nanoparticles in chapter 3.2. EPR analysis was conducted to find the clue of that activity difference. As a result, we found that Mn_5O_8 nanoparticles and micron sized particles have different Mn^{3+} stability during OER catalysis which may cause intrinsic OER property difference between Mn_5O_8 materials. To understand effect of nano size completely, further research should be conducted. We think that understanding effect of crystal structure and nano size on OER activity is important because it will help to develop highly efficient OER catalyst in neutral condition.

References

1. Nocera, D. G. On the future of global energy. *Daedalus* 2006, 135, 112-115.

2. Lewis, N. S.; Nocera, D. G. Powering the planet: Chemical challenges in solar energy utilization. *Proceedings of the National Academy of Sciences* 2006, 103, 15729-15735.

3. Esswein, A. J.; Nocera, D. G. Hydrogen production by molecular photocatalysis. *Chemical reviews* 2007, 107, 4022-4047.

4. Petit, J.-R.; Jouzel, J.; Raynaud, D.; Barkov, N. I.; Barnola, J.-M.; Basile, I.; Bender, M.; Chappellaz, J.; Davis, M.; Delaygue, G. Climate and atmospheric history of the past 420,000 years from the Vostok ice core, Antarctica. *Nature* 1999, 399, 429-436.

5. Sarmiento, J. L.; Le Quere, C. Oceanic carbon dioxide uptake in a model of century-scale global warming. *Science* 1996, 274, 1346-1350.

6. Ronneau, C. *Énergie, pollution de l'air et développement durable*. Presses univ. de Louvain: 2004; Vol. 1.

7. Gandia, L. M.; Arzamedi, G.; Diéguez, P. M. *Renewable hydrogen technologies: Production, purification, storage, applications and safety*. Newnes: 2013.

8. Loll, B.; Kern, J.; Saenger, W.; Zouni, A.; Biesiadka, J. Towards complete cofactor arrangement in the 3.0 Å resolution structure of photosystem II. *Nature* 2005, 438, 1040-1044.

9. Yano, J.; Kern, J.; Sauer, K.; Latimer, M. J.; Pushkar, Y.; Biesiadka, J.; Loll, B.; Saenger, W.; Messinger, J.; Zouni, A.; Yachandra, V. K. Where Water Is Oxidized to Dioxygen: Structure of the Photosynthetic Mn4Ca Cluster. *Science* 2006, 314, 821-825.

10. Ferreira, K. N.; Iverson, T. M.; Maghlaoui, K.; Barber, J.; Iwata, S. Architecture of the Photosynthetic Oxygen-Evolving Center. *Science* 2004, 303, 1831-1838.

11. Umena, Y.; Kawakami, K.; Shen, J.-R.; Kamiya, N. Crystal structure of oxygen-evolving photosystem II at a resolution of 1.9 Å. *Nature* 2011, 473, 55-60.

12. Roelofs, T. A.; Liang, W.; Latimer, M. J.; Cinco, R. M.; Rompel, A.; Andrews, J. C.; Sauer, K.; Yachandra, V. K.; Klein, M. P. Oxidation states of the manganese

cluster during the flash-induced S-state cycle of the photosynthetic oxygen-evolving complex. *Proceedings of the National Academy of Sciences* 1996, 93, 3335-3340.
13. Dau, H.; Iuzzolino, L.; Dittmer, J. The tetra-manganese complex of photosystem II during its redox cycle – X-ray absorption results and mechanistic implications. *Biochimica et Biophysica Acta (BBA) - Bioenergetics* 2001, 1503, 24-39.
14. Tachibana, Y.; Vayssieres, L.; Durrant, J. R. Artificial photosynthesis for solar water-splitting. *Nat Photon* 2012, 6, 511-518.
15. Kanan, M. W.; Nocera, D. G. In Situ Formation of an Oxygen-Evolving Catalyst in Neutral Water Containing Phosphate and Co2+. *Science* 2008, 321, 1072-1075.
16. Betley, T. A.; Wu, Q.; Van Voorhis, T.; Nocera, D. G. Electronic Design Criteria for O−O Bond Formation via Metal−Oxo Complexes. *Inorganic Chemistry* 2008, 47, 1849-1861.
17. Huang, S.-Y.; Ganesan, P.; Jung, W. S.; Cadirov, N.; Popov, B. N. Development of Supported Bifunctional Oxygen Electrocatalysts with High Performance for Unitized Regenerative Fuel Cell Applications. *ECS Transactions* 2010, 33, 1979-1987.
18. Trasatti, S. Electrocatalysis in the anodic evolution of oxygen and chlorine. *Electrochimica Acta* 1984, 29, 1503-1512.
19. Matsumoto, Y.; Sato, E. Electrocatalytic properties of transition metal oxides for oxygen evolution reaction. *Materials Chemistry and Physics* 1986, 14, 397-426.
20. Smith, R. D. L.; Prévot, M. S.; Fagan, R. D.; Zhang, Z.; Sedach, P. A.; Siu, M. K. J.; Trudel, S.; Berlinguette, C. P. Photochemical Route for Accessing Amorphous Metal Oxide Materials for Water Oxidation Catalysis. *Science* 2013, 340, 60-63.
21. Man, I. C.; Su, H.-Y.; Calle-Vallejo, F.; Hansen, H. A.; Martínez, J. I.; Inoglu, N. G.; Kitchin, J.; Jaramillo, T. F.; Nørskov, J. K.; Rossmeisl, J. Universality in Oxygen Evolution Electrocatalysis on Oxide Surfaces. *ChemCatChem* 2011, 3, 1159-1165.
22. Youngblood, W. J.; Lee, S.-H. A.; Kobayashi, Y.; Hernandez-Pagan, E. A.; Hoertz, P. G.; Moore, T. A.; Moore, A. L.; Gust, D.; Mallouk, T. E. Photoassisted Overall Water Splitting in a Visible Light-Absorbing Dye-Sensitized Photoelectrochemical Cell. *Journal of the American Chemical Society* 2009, 131, 926-927.
23. Liu, F.; Concepcion, J. J.; Jurss, J. W.; Cardolaccia, T.; Templeton, J. L.; Meyer, T. J. Mechanisms of Water Oxidation from the Blue Dimer to Photosystem II. *Inorganic*

Chemistry 2008, 47, 1727-1752.

24. Duan, L.; Bozoglian, F.; Mandal, S.; Stewart, B.; Privalov, T.; Llobet, A.; Sun, L. A molecular ruthenium catalyst with water-oxidation activity comparable to that of photosystem II. *Nat Chem* 2012, 4, 418-423.

25. Zhao, Y.; Swierk, J. R.; Megiatto, J. D.; Sherman, B.; Youngblood, W. J.; Qin, D.; Lentz, D. M.; Moore, A. L.; Moore, T. A.; Gust, D.; Mallouk, T. E. Improving the efficiency of water splitting in dye-sensitized solar cells by using a biomimetic electron transfer mediator. *Proceedings of the National Academy of Sciences* 2012, 109, 15612-15616.

26. Gong, M.; Li, Y.; Wang, H.; Liang, Y.; Wu, J. Z.; Zhou, J.; Wang, J.; Regier, T.; Wei, F.; Dai, H. An Advanced Ni–Fe Layered Double Hydroxide Electrocatalyst for Water Oxidation. *Journal of the American Chemical Society* 2013, 135, 8452-8455.

27. McCrory, C. C. L.; Jung, S.; Peters, J. C.; Jaramillo, T. F. Benchmarking Heterogeneous Electrocatalysts for the Oxygen Evolution Reaction. *Journal of the American Chemical Society* 2013, 135, 16977-16987.

28. Yagi, M.; Kaneko, M. Molecular Catalysts for Water Oxidation. *Chemical Reviews* 2000, 101, 21-36.

29. Zhang, M.-T.; Chen, Z.; Kang, P.; Meyer, T. J. Electrocatalytic Water Oxidation with a Copper(II) Polypeptide Complex. *Journal of the American Chemical Society* 2013, 135, 2048-2051.

30. Zhong, D. K.; Cornuz, M.; Sivula, K.; Gratzel, M.; Gamelin, D. R. Photo-assisted electrodeposition of cobalt-phosphate (Co-Pi) catalyst on hematite photoanodes for solar water oxidation. *Energy & Environmental Science* 2011, 4, 1759-1764.

31. Zhong, D. K.; Choi, S.; Gamelin, D. R. Near-Complete Suppression of Surface Recombination in Solar Photoelectrolysis by “Co-Pi” Catalyst-Modified W:BiVO4. *Journal of the American Chemical Society* 2011, 133, 18370-18377.

32. Du, C.; Yang, X.; Mayer, M. T.; Hoyt, H.; Xie, J.; McMahon, G.; Bischoping, G.; Wang, D. Hematite-Based Water Splitting with Low Turn-On Voltages. *Angewandte Chemie International Edition* 2013, 52, 12692-12695.

33. Chen, Z.; Meyer, T. J. Copper(II) Catalysis of Water Oxidation. *Angewandte Chemie International Edition* 2013, 52, 700-703.

34. Kanan, M. W.; Yano, J.; Surendranath, Y.; Dincă, M.; Yachandra, V. K.; Nocera, D. G. Structure and Valency of a Cobalt−Phosphate Water Oxidation Catalyst Determined by in Situ X-ray Spectroscopy. *Journal of the American Chemical Society* 2010, 132, 13692-13701.

35. Dincă, M.; Surendranath, Y.; Nocera, D. G. Nickel-borate oxygen-evolving catalyst that functions under benign conditions. *Proceedings of the National Academy of Sciences* 2010, 107, 10337-10341.

36. Yano, J.; Kern, J.; Sauer, K.; Latimer, M. J.; Pushkar, Y.; Biesiadka, J.; Loll, B.; Saenger, W.; Messinger, J.; Zouni, A. Where water is oxidized to dioxygen: structure of the photosynthetic Mn4Ca cluster. *Science* 2006, 314, 821-825.

37. Fujishima, A.; Honda, K. TiO2 photoelectrochemistry and photocatalysis. *Nature* 1972, 238, 37-38.

38. Hocking, R. K.; Brimblecombe, R.; Chang, L.-Y.; Singh, A.; Cheah, M. H.; Glover, C.; Casey, W. H.; Spiccia, L. Water-oxidation catalysis by manganese in a geochemical-like cycle. *Nat Chem* 2011, 3, 461-466.

39. Ruettinger, W. F.; Ho, D. M.; Dismukes, G. C. Protonation and Dehydration Reactions of the Mn4O4L6 Cubane and Synthesis and Crystal Structure of the Oxidized Cubane [Mn4O4L6]+: A Model for the Photosynthetic Water Oxidizing Complex. *Inorganic Chemistry* 1999, 38, 1036-1037.

40. Kanady, J. S.; Tsui, E. Y.; Day, M. W.; Agapie, T. A Synthetic Model of the Mn3Ca Subsite of the Oxygen-Evolving Complex in Photosystem II. *Science* 2011, 333, 733-736.

41. Tsui, E. Y.; Tran, R.; Yano, J.; Agapie, T. Redox-inactive metals modulate the reduction potential in heterometallic manganese–oxido clusters. *Nat Chem* 2013, 5, 293-299.

42. Najafpour, M. M.; Ehrenberg, T.; Wiechen, M.; Kurz, P. Calcium Manganese(III) Oxides (CaMn2O4·x H2O) as Biomimetic Oxygen-Evolving Catalysts. *Angewandte Chemie International Edition* 2010, 49, 2233-2237.

43. Brimblecombe, R.; Kolling, D. R. J.; Bond, A. M.; Dismukes, G. C.; Swiegers, G. F.; Spiccia, L. Sustained Water Oxidation by [Mn4O4]7+ Core Complexes Inspired by Oxygenic Photosynthesis. *Inorganic Chemistry* 2009, 48, 7269-7279.

44. Indra, A.; Menezes, P. W.; Zaharieva, I.; Baktash, E.; Pfrommer, J.; Schwarze, M.; Dau, H.; Driess, M. Active Mixed-Valent MnOx Water Oxidation Catalysts through Partial Oxidation (Corrosion) of Nanostructured MnO Particles. *Angewandte Chemie International Edition* 2013, 52, 13206-13210.

45. Menezes, P. W.; Indra, A.; Littlewood, P.; Schwarze, M.; Göbel, C.; Schomäcker, R.; Driess, M. Nanostructured Manganese Oxides as Highly Active Water Oxidation Catalysts: A Boost from Manganese Precursor Chemistry. *ChemSusChem* 2014, 7, 2202-2211.

46. Kuo, C.-H.; Mosa, I.; Poyraz, A. S.; Biswas, S.; El-Sawy, A. M.; Song, W.; Luo, Z.; Chen, S.-Y.; Rusling, J. F.; He, J. Robust Mesoporous Manganese Oxide Catalysts for Water Oxidation. *ACS Catalysis* 2015.

47. Takashima, T.; Hashimoto, K.; Nakamura, R. Mechanisms of pH-Dependent Activity for Water Oxidation to Molecular Oxygen by MnO2 Electrocatalysts. *Journal of the American Chemical Society* 2011, 134, 1519-1527.

48. Takashima, T.; Hashimoto, K.; Nakamura, R. Inhibition of Charge Disproportionation of MnO2 Electrocatalysts for Efficient Water Oxidation under Neutral Conditions. *Journal of the American Chemical Society* 2012, 134, 18153-18156.

49. Robinson, D. M.; Go, Y. B.; Greenblatt, M.; Dismukes, G. C. Water Oxidation by λ-MnO2: Catalysis by the Cubical Mn4O4 Subcluster Obtained by Delithiation of Spinel LiMn2O4. *Journal of the American Chemical Society* 2010, 132, 11467-11469.

50. Zaharieva, I.; Chernev, P.; Risch, M.; Klingan, K.; Kohlhoff, M.; Fischer, A.; Dau, H. Electrosynthesis, functional, and structural characterization of a water-oxidizing manganese oxide. *Energy & Environmental Science* 2012, 5, 7081-7089.

51. Gorlin, Y.; Jaramillo, T. F. A Bifunctional Nonprecious Metal Catalyst for Oxygen Reduction and Water Oxidation. *Journal of the American Chemical Society* 2010, 132, 13612-13614.

52. Frey, C. E.; Kurz, P. Water oxidation catalysis by synthetic manganese oxides with different structural motifs: a comparative study. *Chemistry–A European Journal* 2015, 21, 14958-14968.

53. Robinson, D. M.; Go, Y. B.; Mui, M.; Gardner, G.; Zhang, Z.; Mastrogiovanni, D.;

Garfunkel, E.; Li, J.; Greenblatt, M.; Dismukes, G. C. Photochemical Water Oxidation by Crystalline Polymorphs of Manganese Oxides: Structural Requirements for Catalysis. *Journal of the American Chemical Society* 2013, 135, 3494-3501.

54. Iyer, A.; Del-Pilar, J.; King'ondu, C. K.; Kissel, E.; Garces, H. F.; Huang, H.; El-Sawy, A. M.; Dutta, P. K.; Suib, S. L. Water oxidation catalysis using amorphous manganese oxides, octahedral molecular sieves (OMS-2), and octahedral layered (OL-1) manganese oxide structures. *The Journal of Physical Chemistry C* 2012, 116, 6474-6483.

55. Meng, Y.; Song, W.; Huang, H.; Ren, Z.; Chen, S.-Y.; Suib, S. L. Structure–property relationship of bifunctional MnO2 nanostructures: highly efficient, ultra-stable electrochemical water oxidation and oxygen reduction reaction catalysts identified in alkaline media. *Journal of the American Chemical Society* 2014, 136, 11452-11464.

56. Jin, K.; Park, J.; Lee, J.; Yang, K. D.; Pradhan, G. K.; Sim, U.; Jeong, D.; Jang, H. L.; Park, S.; Kim, D.; Sung, N.-E.; Kim, S. H.; Han, S.; Nam, K. T. Hydrated Manganese(II) Phosphate (Mn3(PO4)2·3H2O) as a Water Oxidation Catalyst. *Journal of the American Chemical Society* 2014, 136, 7435-7443.

57. Park, J.; Kim, H.; Jin, K.; Lee, B. J.; Park, Y.-S.; Kim, H.; Park, I.; Yang, K. D.; Jeong, H.-Y.; Kim, J.; Hong, K. T.; Jang, H. W.; Kang, K.; Nam, K. T. A New Water Oxidation Catalyst: Lithium Manganese Pyrophosphate with Tunable Mn Valency. *Journal of the American Chemical Society* 2014, 136, 4201-4211.

58. Jin, K.; Chu, A.; Park, J.; Jeong, D.; Jerng, S. E.; Sim, U.; Jeong, H.-Y.; Lee, C. W.; Park, Y.-S.; Yang, K. D.; Kumar Pradhan, G.; Kim, D.; Sung, N.-E.; Hee Kim, S.; Nam, K. T. Partially Oxidized Sub-10 nm MnO Nanocrystals with High Activity for Water Oxidation Catalysis. *Sci. Rep.* 2015, 5.

59. An, K.; Park, M.; Yu, J. H.; Na, H. B.; Lee, N.; Park, J.; Choi, S. H.; Song, I. C.; Moon, W. K.; Hyeon, T. Synthesis of uniformly sized manganese oxide nanocrystals with various sizes and shapes and characterization of their T1 magnetic resonance relaxivity. *European Journal of Inorganic Chemistry* 2012, 2012, 2148-2155.

국 문 초 록

미래의 유력한 대체에너지원인 수소를 효율적으로 생산하기 위해서는 성능이 좋은 물 산화 촉매가 필요하다. 이를 위하여 다양한 벌크 스케일의 망간 촉매들이 개발, 연구되어왔다. 그러나 기존의 망간 산화물 촉매들은 중성 조건에서 특성이 좋지 않다는 한계를 가지고 있었다. 그래서 우리 그룹에서는 최근 부분 산화된 MnO 나노입자를 합성함으로써 중성조건에서도 특성이 뛰어난 물 산화 촉매를 개발하여 기존 망간 산화물 촉매의 한계를 극복하였다.

그래서 본 연구에서는 기존 연구들에서 다뤘던 벌크 스케일의 물질이 아닌 나노 스케일의 물질에서 결정구조가 물 산화 촉매특성에 미치는 영향을 명확하게 살펴봄으로써 나노입자 촉매의 특성을 더욱 향상시키고자 하였다. 이를 위하여 나노입자간의 외형은 최대한 유지하면서 결정 구조만 변화시켜 다양한 망간 산화물 나노 입자(Mn_3O_4, Mn_5O_8, Mn_2O_3)들을 합성하였다. 망간 산화물 나노입자들의 촉매 특성은 cyclic voltammetry를 통해 평가되었다. 그 결과 놀랍게도, 벌크입자와는 달리 부분산화된 MnO, Mn_3O_4와 Mn_2O_3 나노입자의 경우 유사한 촉매 특성을 보여주었고, Mn_5O_8 나노입자의 경우만 조금 더 낮은 촉매 특성을 보여주었다. 이는 결정구조에 따라 명확한 특성차이를 보여주는 벌크 망간 산화물과는 달리, 입자의 사이즈가 나노화 되면서 결정구조가 촉매 특성에 미치는 영향력이 감소했음을 보여준다. 한편, Mn_5O_8 나노입자의 경우 다른 입자들과는 다른 촉매 특성을 보여주었는데, 우리는 이러한 촉매 특성차이가 무엇으로부터 기인하는지 알아내기

위하여 촉매의 물 분해 메커니즘에 대한 단서를 얻을 수 있는 Electrokinetics study와 redox peak 분석을 진행하였다. 그 결과, 부분산화된 MnO, Mn_3O_4와 Mn_2O_3 나노입자의 물 분해 메커니즘(속도결정단계 직전 반응에서 전자 1개, 수소 이온 1개 관여)과는 달리 Mn_5O_8 나노 입자는 속도결정단계 직전 반응에서 전자 1개와 수소 이온이 2개 관여하는 메커니즘을 보여주었고, 이러한 다른 물 분해 메커니즘으로 인해 다른 촉매 특성을 가지는 것으로 생각된다.

다음으로, 우리는 앞서 합성한 다양한 결정구조의 망간 산화물 나노입자들이 동일상의 벌크입자들보다 물 산화 촉매특성이 훨씬 뛰어남을 확인하였다. 그래서 우리는 한번도 물 산화 촉매로서 연구된 적이 없는 Mn_5O_8을 통해 망간 산화물 나노입자와 벌크입자의 차이가 무엇으로부터 기인하는지 밝혀내기 위한 연구를 진행하였다. BET분석과 단위 질량으로 환산한 촉매 특성 비교를 통해서 우리는 표면적의 영향을 제외하고도 Mn_5O_8 나노입자가 Mn_5O_8 마이크로입자보다 훨씬 뛰어난 촉매 특성을 지니고 있고, 더 나아가 촉매 안정성 역시 뛰어남을 확인하였다. 이러한 결과들은 입자의 사이즈가 나노화되면서 촉매의 본질적인 특성이 바뀔 수 있음을 암시한다. 우리는 이러한 촉매 특성 차이의 원인에 대한 실마리를 찾기 위하여, EPR 분석을 통해 Mn_5O_8 물질의 산화수 거동을 살펴보았다. 그 결과, 우리는 Mn_5O_8 나노입자가 마이크로입자에 비해 물 분해 중에 Mn^{3+}가 더 안정함을 확인할 수 있었고, 이는 물 분해 중 Mn^{3+}의 안정성이 사이즈가 다른 두 Mn_5O_8 재료의 본질적인 촉매 특성 차이를 야기했을 가능성을 보여준다.

본 연구를 통해서 나노 스케일에서 결정구조가 촉매 특성에

미치는 영향과 입자 사이즈의 나노화가 물 분해 촉매 특성에 미치는 영향에 대해 이해할 수 있었다. 이러한 결과들은 중성조건에서 더욱 뛰어난 특성을 지닌 나노 촉매입자를 개발하는데 있어서 의미 있는 첫 걸음이 될 것이라고 생각하며, 추후 나노 스케일에서 결정구조와 입자 사이즈 나노화의 영향을 더 명확히 이해하기 위한 연구가 진행되어야 한다.

주요어: 산소 발생 반응, 전기 촉매, 망간 산화물, 나노입자, 결정 구조

학 번: 2014-21462